The magnitude of equilibrium isotope fractionation of Mg between forsterite, diopside and melt at liquidus temperatures.

Bram de Winter[a,*], Andrew M. Walker[a], Elena Melekhova[a], Xiao-Ning Liu[b], Tim Elliott[b],

[a] Department of Earth Sciences, University of Oxford, South Parks Road, Oxford, OX1 3AN, UK

[b] School of Earth Sciences, University of Bristol, Wills Memorial Building, Queen's Road, Bristol, BS8 1RJ, UK

[*]Corresponding Author, bram.dewinter@earth.ox.ac.uk

This manuscript is under review at Geochimica et Cosmochimica Acta

The magnitude of equilibrium isotope fractionation of Mg between forsterite, diopside and melt at liquidus temperatures.

Bram de Winter[a,*], Andrew M. Walker[a], Elena Melekhova[a], Xiao-Ning Liu[b], Tim Elliott[b],

[a] *Department of Earth Sciences, University of Oxford, South Parks Road, Oxford, OX1 3AN, UK*

[b] *School of Earth Sciences, University of Bristol, Wills Memorial Building, Queen's Road, Bristol, BS8 1RJ, UK*

[*] *Corresponding Author, bram.dewinter@earth.ox.ac.uk*

Abstract

We examine the equilibrium fractionation of Mg isotopes between forsterite, diopside, and a coexisting melt at liquidus temperatures using a combination of analyses of petrological-experiment products and atomic-scale simulations. Our experiment yields $\Delta^{26}Mg_{ol/melt}$ = -0.058 ± 0.032 ‰ (2s.e.) and $\Delta^{26}Mg_{cpx/melt}$ = 0.060 ± 0.034 ‰ (2s.e.) for crystals grown from a near-cotectic basaltic melt in the CMAS system, which combine to give $\Delta^{26}Mg_{cpx/ol}$ = 0.131 ± 0.045 ‰ at 1300 °C. The value of $\Delta^{26}Mg_{ol/melt}$ is within the uncertainty of the mean olivine-melt fractionation determined for unzoned phenocrysts and naturally quenched glass from ocean island and mid-ocean ridge basalts. We compare the experimentally determined Mg isotope fractionation between olivine and clinopyroxene with *ab initio* calculations using different DFT functionals. We demonstrate that when using the revised Perdew–Burke–Ernzerhof (PBESOL) exchange-correlation functional, accounting for thermal expansion, and site-averaging for forsterite, our ab initio results are in good agreement with our experiments, yielding $\Delta^{26}Mg_{cpx/ol}$ = 0.134‰ at 1300°C. Using the Local Density Approximation (LDA) or other Generalised Gradient Approximation (GGA) functionals, or neglecting thermal expansion, lowers $\Delta^{26}Mg_{cpx/ol}$ values to approximately 0.03–0.06 ‰ below the experimentally measured values. Neglecting site-averaging in forsterite results in positive (using only M1) or negative (using only M2) deviations in fractionation of 0.08‰ from averaged isotope ratios. Comparison of

our experimentally and theoretically derived $\Delta^{26}Mg_{cpx/ol}$ values with empirical estimates from natural samples reveals a systematic offset, underscoring the need to distinguish equilibrium mineral–mineral fractionation from empirically derived relationships that may incorporate kinetic or compositional effects.

Keywords: Mg isotopes, equilibrium isotope fractionation, density functional theory, high-temperature experiments.

1. Introduction

Atomic-scale simulations are increasingly used to provide information on isotopic fractionation driven by deep-Earth and planetary processes (e.g Young et al., 2015). Validating these simulations has been challenging due to the small, predicted effects (Blanchard et al., 2017; Schauble, 2011) relative to the limits of traditional analytical reproducibility and the difficulty of acquiring suitable natural samples or experiments that demonstrate pure equilibrium isotope fractionation. Here, we focus on the relatively simple case of equilibrium fractionation of magnesium isotopes between high-temperature silicate phases at ambient pressure. Magnesium is a major rock-forming element, representing a fundamental building block of geological reservoirs. The stable isotopes of magnesium (approx. 79% ^{24}Mg, 10% ^{25}Mg, 11% ^{26}Mg) exhibit a notable relative mass difference of up to 8%, which promotes significant isotopic fractionation, as has been documented in igneous systems that can operate on planetary scales (Hin et al., 2017; Sedaghatpour & Teng, 2016; Teng et al., 2010).

Atomic-scale simulations based on density functional theory (DFT) suggest significant equilibrium fractionation of Mg isotopes among major mantle minerals (e.g. Huang et al., 2013; Schauble, 2011; Wang et al., 2023), broadly consistent with observations of Mg isotopic differences in apparently equilibrated natural samples (Young et al., 2009). While such simulations are ideally *ab initio* (i.e., based on first principles without adjustable parameters),

important choices must be made that may affect their reliability. For example, it is necessary to choose the exchange-correlation functional and to decide how to incorporate thermal expansion or the presence of different crystallographic sites in the minerals being studied. Previous studies have made use of the local density approximation (LDA; Perdew & Zunger, 1981) or the PBE (PBE; Perdew et al., 1996), semi-local generalised gradient approximation (GGA) for exchange-correlation functional, but newer functionals are now routinely available (e.g. PBESOL; Perdew et al., 2008). PBESOL was created to model the equilibrium properties of solids better and has proven to more accurately reproduce the lattice parameters and elastic properties of silicate minerals than previous GGA functionals. Moreover, many studies have overlooked the effect of thermal expansion. Wang et al. (2023) demonstrate that thermal expansion alters the equilibrium fractionation of Mg isotopes between different minerals. Given the sensitivity of equilibrium isotope fractionation to both exchange-correlation functional and thermal expansion, thorough validation against well-constrained measurements is needed.

Analysis of natural samples, including inter-mineral Mg isotope fractionations preserved in mantle peridotites, as well as mineral-melt isotope fractionations recorded in mid-ocean ridge basalts (MORB), ocean island basalts (OIB), and chondritic meteorites, has provided an empirical foundation for understanding high-temperature isotope fractionation in planetary materials (e.g. Pogge von Strandmann et al., 2011; Stracke et al., 2018; Teng et al., 2010; Yang et al., 2009). Early studies provided valuable information but were limited in their ability to resolve these effects because equilibrium fractionations at magmatic temperatures are small and approach the precision limits of sample-standard bracketing techniques (Teng et al., 2015). Recent development of the critical mixture double-spiking technique (Coath et al., 2017) has substantially improved analytical reproducibility, enabling more robust detection of subtle Mg

isotope fractionations (Liu et al., 2023) and small but significant Mg isotope differences between chondrites and Earth (Hin et al., 2017).

Interpreting isotopic variations requires well-constrained equilibrium fractionation factors, especially the key equilibrium melt-solid fractionation factors. Particularly, the recent argument of the widely occurring diffusion-driven Mg isotope fractionations in the MORB samples was based mainly on the empirically determined non-zero melt-olivine fractionation factor (Liu et al., 2024, EPSL), while others, adopting a zero value of melt-olivine fractionation factor, concluded equilibrium isotope fractionations (Soderman et al., 2024). Despite this, a non-zero melt-olivine fractionation factor was carefully determined previously (Liu et al., 2022) given the difficulties in obtaining fully equilibrated glass-mineral pairs from natural samples and the fact that diffusion processes can easily influence Mg isotopes (Lai et al., 2015; Richter et al., 2009; Teng et al., 2011), further constrains from theoretical prediction, and petrological experimental work are necessary. Direct comparison between measured Mg isotope fractionation in natural samples and ab initio calculations of equilibrium fractionation remains nontrivial.

Petrological experiments offer an alternative method for studying equilibrium isotope fractionation, as they theoretically enable control over key variables like temperature, pressure, and composition. However, in practice, this potential is not always achieved because experimental samples, like natural ones, can experience kinetic fractionation, especially in the form of Soret diffusion, caused by temperature gradients within the experiments, as reported by Liu et al. (2022). The Soret effect is a thermodiffusion process in which isotopes migrate along a temperature gradient, with heavier isotopes tending to concentrate on the cooler side and can impose very significant isotopic fractionations (Richter et al., 2008). To address this, experiments should explicitly aim to minimise kinetic effects by ensuring minimal thermal gradients across the experimental charge and by homogenising initial compositions. The

current lack of controlled studies that can truly isolate equilibrium isotope fractionation between major silicate minerals and co-existing melt highlights the necessity for such research.

This study assesses the influence of various DFT parameters on calculated equilibrium isotope fractionation factors for Mg between forsterite-melt, diopside-melt, and forsterite-diopside, by comparing modelling results with experimental results. Forsterite and diopside were synthesised at near-liquidus conditions at 1 atm in the CMAS system (Ca-Mg-Al-Si). Additionally, DFT calculations are performed from 0 to 4000 K at 1 atm, using different exchange-correlation functionals, site-averaging methods, and thermal expansion factors (following the approach of Walker et al. (2025)) to calculate isotopic differences between forsterite and diopside. These paired experimental and theoretical results provide a basis for evaluating Mg isotope fractionation at high temperatures.

2. Methods

We use two complementary methods to assess equilibrium Mg isotope fractionation between forsterite and diopside. We do this because atomic-scale simulations are most reliable for fractionation between crystalline solids; in this case, the fractionation is driven by mass-dependent changes in crystal vibrations, which lattice dynamics can describe. This approach is not directly applicable to liquids. In our first approach, we used samples from a pair of experiments in which we grew forsterite or diopside crystals from a melt composition at a temperature designed to leave a residual melt near the CMAS cotectic. We measured $\Delta^{26}Mg_{ol/melt}$ and $\Delta^{26}Mg_{cpx/melt}$. Because the residual melt compositions are similar, we can use these experiments to determine $\Delta^{26}Mg_{cpx/ol}$. Since diopside and forsterite are endmembers of clinopyroxene (cpx) and olivine (ol), we label this fractionation as $\Delta^{26}Mg_{cpx/ol}$ (eq. 1) throughout the text for consistency with literature conventions:

$$\Delta^{26}\mathrm{Mg}_{\frac{\mathrm{cpx}}{\mathrm{ol}}} = \Delta^{26}\mathrm{Mg}_{\frac{cpx}{\mathrm{melt}}} - \Delta^{26}\mathrm{Mg}_{\frac{\mathrm{ol}}{\mathrm{melt}}} =$$

$$\left(\frac{\frac{^{26}Mg}{^{24}\mathrm{Mg}_{\mathrm{cpx}}}}{\frac{^{26}Mg}{^{24}\mathrm{Mg}_{\mathrm{melt}}}}\right) - \left(\frac{\frac{^{26}Mg}{^{24}\mathrm{Mg}_{ol}}}{\frac{^{26}Mg}{^{24}\mathrm{Mg}_{\mathrm{melt}}}}\right) \quad (1)$$

Our experiments are designed to minimise the influence of non-equilibrium isotope fractionation processes. We aimed to eliminate the effects of Soret diffusion and Fe-Mg interdiffusion by working in an iron-free system with minimal temperature gradients to minimize soret diffusion, and by using long durations to ensure phase homogeneity. With this approach, we create a situation designed to achieve near-equilibrium isotope fractionation.

In our second approach, we utilise atomic-scale simulations to constrain the equilibrium fractionation of ^{24}Mg relative to ^{26}Mg in cpx and ol as a function of temperature. By design, these simulations yield only equilibrium fractionation and are not sensitive to other processes that cause isotopic fractionation. In this approach, $\Delta^{26}\mathrm{Mg}_{\mathrm{cpx/ol}}$ is derived from the reduced partition function, ß (X, ^{24}Mg, ^{26}Mg), which is the equilibrium constant for the isotopic exchange reaction between the phase of interest, X, and an ideal gas (Urey, 1947). The equilibrium isotope fractionation factor, between two solid mineral phases (cpx and ol) and two isotopes of an element (^{24}Mg, ^{26}Mg) can be determined as the ratio of ß (X, ^{24}Mg, ^{26}Mg), or as reduced partition functions or as the difference in expected measured isotopic content:

$$\Delta^{26}Mg_{\frac{cpx}{ol}}(DFT) \approx (\ln(\beta(\mathrm{Di}, ^{24}Mg, ^{26}Mg) - \ln(\beta(\mathrm{Fo}, ^{24}Mg, ^{26}Mg)) \quad (2)$$

where $\Delta^{26}\mathrm{Mg}_{\mathrm{cpx/ol}}$ is the isotopic difference between cpx and ol. In our calculations, β is obtained from the phonon density of states via atomic-scale simulations. However, important choices must be made when undertaking these calculations, and these have not been directly compared with isotopic measurements. Our combined approach offers an opportunity to

explore the impact of these choices and to validate the overall computational approach in situations where experiments are more challenging.

2.1 Experiments

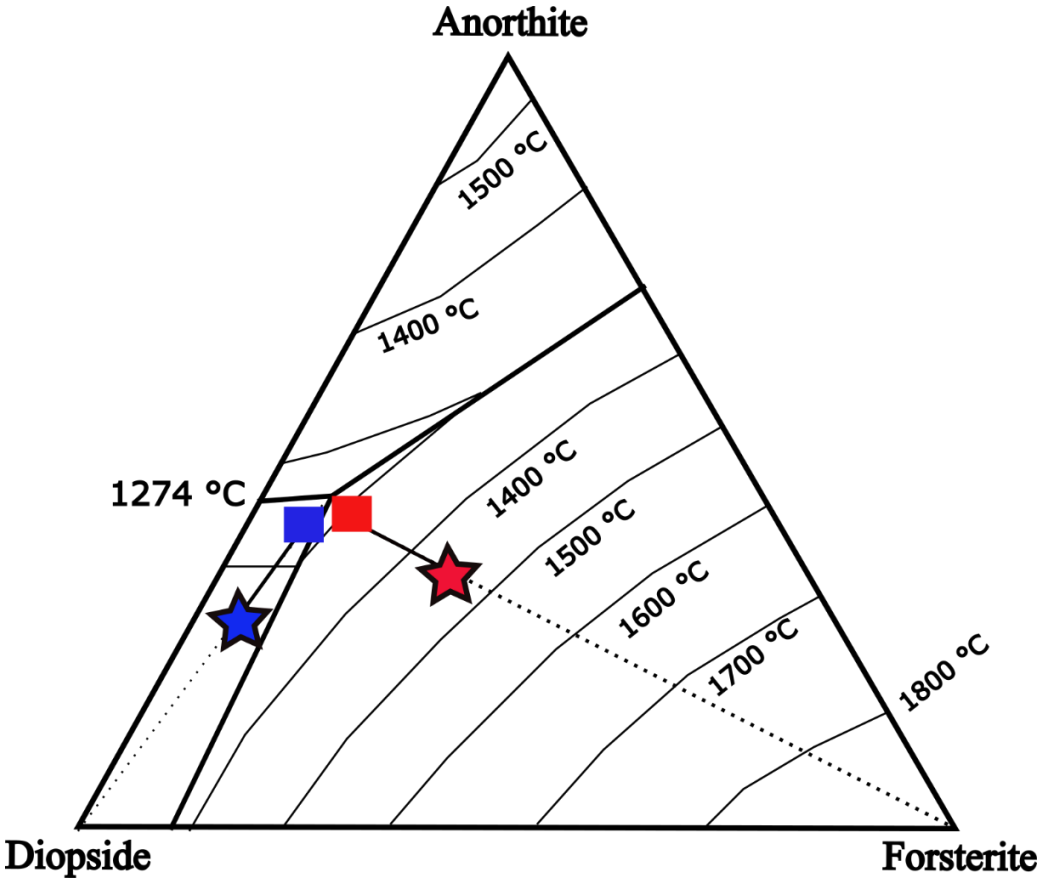

Figure 1, Ternary diagram of Diopside-Anorthite-Forsterite after Morse (1980). Starting composition (stars) and the measured residual melt (squares) are joined by tie lines for experiments that crystallise diopside (blue) and forsterite (red).

We synthesised forsterite and diopside crystals from starting compositions within the CaO-MgO-Al2O3-SiO_2 (CMAS) system. We selected starting compositions and equilibration temperatures near the liquidus to achieve melt fractions of 65 vol.% and 80 vol.% for diopside and forsterite experiments, respectively, to keep the residual melt composition close to the eutectic (Figure 1).

149 Starting compositions were synthesised using high-purity oxide and carbonate reagents:
150 calcium oxide (CaO), magnesium oxide (MgO), aluminium oxide (Al_2O_3), silicon dioxide
151 (SiO_2), and calcium carbonate ($CaCO_3$). All oxides were subjected to a drying process at
152 1000°C for 12 hours to eliminate any absorbed moisture (H_2O). The dried oxides and
153 carbonates were then accurately weighed, mixed and ground for 30 minutes to ensure a uniform
154 distribution of components. Following this grinding, $CaCO_3$ was added, and the starting
155 mixture was then decarbonated at 1000°C overnight. After decarbonation, the mixture was
156 subjected to a second grinding to enhance homogeneity. Starting composition mixtures were
157 glassed at 1375°C for glass BDW-S2 (used to grow Di) and 1500°C for glass BDW-S1 (used
158 to grow Fo) for 2 hours in a Gera vertical box furnace (HTRV 70-250/18) at the Earth Science
159 Department of the University of Oxford. Subsequently, the glassed starting composition were
160 quenched in water. To ensure a consistent and homogeneous starting composition, two cycles
161 of melting and grinding were performed (Table 1).

Table 1. Experimental starting composition measured by EPMA at the University of Oxford. Elemental concentrations are given as wt% oxide.

Experiment	n^a	MgO	s.d	SiO_2	s.d	Al_2O_3	s.d	CaO	s.d	Total
BDW-S2 (Di)	12	15.43	0.17	50.86	0.22	10.36	0.13	22.96	0.13	99.62
BDW-S1 (Fo)	25	21.36	0.13	47.15	0.18	12.37	0.1	17.59	0.09	99.47

[a]*Compositions are given as the average of n analyses.*

162

163 The crystal growth experiments were conducted in a vertical furnace under atmospheric
164 pressure in air. A "chandelier" assembly was designed to accommodate four platinum loops,
165 each containing a mixture of starting material and a small amount of PVA glue to ensure
166 attachment of the starting material to the loop. In prior experiments, the hot spot and
167 temperature gradient in the furnace were carefully calibrated. We observed a 2 °C temperature
168 gradient over a 10 cm vertical distance within the hotspot using an external Type B
169 thermocouple. The beads in our setup are spaced 1 cm apart. Assuming similar thermal

gradients along the horizontal axis, we expect temperatures to vary by <0.2 °C between beads within a single experiment.

A "chandelier" was positioned at the vertical hotspot at 1500 ± 2.5 °C for 2 hours to ensure thermal equilibration. Subsequently, the temperature was gradually decreased to the target endpoint at a controlled rate of 1 °C/min, as outlined by Mallmann & O'Neill (2009). The furnace was then held at the final temperature (Table 2) for seven days to allow the growth of crystals exceeding 100 μm. The experiments were quenched in water. Subsequently, the quench beads were extracted, mounted in Araldite epoxy resin, and first polished with abrasive paper and then with a series of diamond pastes. In Figure 2, we present backscattered SEM images of two run products, BDW-S2-1 (Di) and BDW-S1-4 (Fo).

The experimental numbering scheme sequentially indicates: the starting composition (BDW-S1 or BDW-S2), the experimental run (e.g., BDW-S2-1), the bead from each experimental run (e.g., BDW-S2-1-1), and a letter for the individual drill site (e.g., BDW-S2-1-1A).

2.2 Analytical techniques

The morphology and size of recovered forsterite and diopside crystals were determined using a FEI Quanta 650 scanning electron microscope (SEM) at the Department of Earth Sciences, University of Oxford. Backscatter images of all recovered beads are given in Supplementary Figure S1-1.

The major element compositions of starting compositions and experimental run products were analysed by Electron Microprobe Analysis (EMPA) using a CAMECA SX-5 FE system at the University of Oxford's Department of Earth Sciences, operating at 10 nA and 20 kV with a spot size of 1 μm. For calibration, we used natural albite (Si, Al, Mg) and andradite (Ca) standards. To ensure that experimental run products are homogeneous, transect lines were set up across minerals and melt pools (see Supplementary Figure S1-2).

For magnesium isotope analysis, beads BDW-S1-4 (Fo) and BDW-S2-1 (Di) were chosen because they contained the largest mineral phases (Supplementary Figure S1-1). The material drilling and isotope analysis follow the procedures detailed by Liu et al. (2022, 2023). In brief, a New Wave Research microdrill was used to obtain two samples each of forsterite and diopside, as well as four samples of silicate melt from BDW-S2-1 (Di) and two from BDW-S1-4 (Fo). The sample material was drilled in a droplet of approximately 5 μL of Milli-Q water placed on the surface mount. The water containing the drilled powder was then recovered using a pipettor and transferred to a cleaned Teflon beaker. The drilled samples were subsequently digested in a mixture of ultra-pure concentrated HNO_3, HCl, and HF in a 3:1:1 volume ratio on a hotplate at 150 °C. Following complete digestion, the samples were dissolved in 1 M HNO_3 for magnesium column chemistry. Magnesium was purified using two-column cation-exchange chromatography with BioRad AG50W-X12 resin. Aliquots of 1 mL of eluent were taken before and after the Mg collection window to check the yield, which exceeded 99.8% for all samples. Magnesium isotope measurements were performed on a Thermo-Finnigan Neptune MC-ICPMS. Jet sample cone and H skimmer cone were used. The sample solution was aspirated into the mass spectrometer in a 0.3 M HNO3 solution containing 1 μg/ml Mg, using the combination of a Savillex PFA nebuliser and Apex HF (Element Inc.). The Instrumental mass bias is corrected through the ^{25}Mg-^{26}Mg critical mixture double spike method (Coath et al., 2017; Hin et al., 2017; Liu et al., 2023). Mg isotope data are reported as $\delta^{26}Mg_{DSM-3}$ (the relative difference of $^{26}Mg/^{24}Mg$ between the sample and the reference standard DSM-3), and are subsequently abbreviated as $\delta^{26}Mg$. Analyses of the rock standard BHVO-2 and BIR-1 yielded a $\delta^{26}Mg$ value of -0.206±0.035‰ and -0.206±0.023‰, respectively, consistent with the previous reports (He et al., 2022; Liu et al., 2023)

2.3 First-principles calculations

The *ab initio* approach for isotope fractionation is similar to previous studies of Mg isotope fractionation (Huang et al., 2013; Schauble, 2011; Wang et al., 2023; Wu et al., 2015; Young et al., 2009) as well as other isotope systems (Blanchard et al., 2009; Javoy et al., 2012; Li et al., 2009; Li & Liu, 2011; Rustad & Dixon, 2009). To calculate $\Delta^{26}Mg_{cpx/ol}$, we use plane waves and pseudopotential (Payne et al., 1992) approach to density functional theory (DFT: Hohenberg & Kohn, 1964; Kohn & Sham, 1965) and lattice dynamics in CASTEP (Clark et al., 2005). Our reference calculations are undertaken in two steps. First, we determine the equilibrium structure of forsterite and diopside. These calculations were performed using a generalised gradient approximation functional designed to give improved equilibrium properties of solids (PBESOL; Perdew et al., 2008), and initial crystal structures of forsterite and diopside were obtained from the American Mineralogist Crystal Structure Database (Downs & Hall-Wallace, 2003). These structures were refined by minimising the static energy with respect to atomic positions and cell parameters, with convergence assumed when the maximum force on each atom was below 1.0×10^{-4} eV/ang, maximum stress 0.05 GPa and total energy changes less than 1.0×10^{-5} eV. All our calculations were performed with norm-conserving pseudopotentials for core electrons and the 2p electrons for O, the 3s and 3p electrons for Si, and the 3s electrons for Ca and Mg included in the valence. The electron density was expanded on a plane-wave basis with a cutoff energy of 1000 eV and sampled in reciprocal space with 4×2×4 and 4×4×2 Monkhorst-Pack grids (Monkhorst & Pack, 1976) for forsterite and diopside, respectively (these parameters were chosen by convergence testing of the phonon frequencies).

In the second step, we calculate the phonon frequencies of both minerals with one magnesium atom substituted for either the heavy (^{26}Mg) or light (^{24}Mg) isotope and the masses of all other atoms set according to their natural isotopic abundances. We used variational Density Functional Perturbation Theory (DFPT: Gonze, 1997; Gonze & Lee, 1997; Refson et al., 2006)

to calculate phonon frequencies on a shifted grid (to include the gamma point) in reciprocal space, as used for the expansion of the electronic wavefunctions. These were supplemented using Fourier interpolation (Giannozzi et al., 1991) to interpolate frequencies at wave vectors between those included in the DFPT calculation. We calculated the ß (X, Y, Y*) for diopside and forsterite:

$$\beta(\mathrm{X},\mathrm{Y},\mathrm{Y}^{*}) = \prod_{\mathrm{i}=1}^{\mathrm{n^q}} \left[\prod_{\mathrm{j}=1}^{3\mathrm{N^{at}}} \left(\frac{\omega^{*}_{i,j}}{\omega_{i,j}} \frac{\mathrm{e}^{-\mathrm{h}\omega^{*}_{\mathrm{i,j}}/(2\mathrm{kT})}}{1-\mathrm{e}^{-\mathrm{h}\omega^{*}_{\mathrm{i,j}}/(2\mathrm{kT})}} \frac{1-\mathrm{e}^{-\mathrm{h}\omega_{\mathrm{i,j}}/(2\mathrm{kT})}}{\mathrm{e}^{-\mathrm{h}\omega_{i,\mathrm{j}}/(2\mathrm{kT})}} \right) \right]^{w_i} \qquad (3)$$

(Kieffer, 1982; Schauble, 2004), where $\omega_{i,j}$ and $\omega^{*}_{i,j}$ are the vibrational frequencies calculated for the two different isotopes in phase X at the i^{th} reciprocal lattice sampling point for j^{th} branch within the simulation cell that contains N_{at} atoms in the crystal unit cell. T is the temperature in Kelvin, and k is Boltzmann's constant. At a large grid of N^{q} points sampled in the first Brillouin Zone, we run the second product of Eq. (3) over all modes. We utilised the symmetry of the reciprocal lattice to reduce computational costs. This symmetry is applied to equivalent points with weighting factors w_i, ensuring proper accounting for points on the edges of the sampled irreducible volume. The aim is, therefore, to compute $\omega_{i,j}$ and $\omega^{*}_{i,j}$ with enough accuracy within the available computational limitations.

The reference calculations are supplemented by others where different choices are made for the calculation of equilibrium isotope fractionation. We alter the exchange correlation functional using the LDA (Perdew & Zunger, 1981), or a common generalised gradient approximation due to PBE (Perdew et al., 1996). We also explore altering the site in forsterite where the Mg isotope substitution is made. Duan et al. (2023) show that accounting for the presence of two different Mg sites in forsterite is important when calculating isotope

fractionation factors. These sites have different polyhedron volumes, affecting isotope fractionation up to 0.5‰ at 900 K (Duan et al., 2023).

Finally, we account for the thermal expansion of the forsterite and diopside crystals. In this study, we employ the approach described by Walker et al. (2025) to investigate the differential thermal expansion of forsterite and also apply it to diopside. For each cell volume, V (calculated by performing geometry optimisation with various pressures while neglecting temperature effects), we calculate phonon frequencies to evaluate the Helmholtz free energy. The volume-energy data obtained are used to fit isothermal third-order Birch-Murnaghan equations of state (EOS), incorporating temperature dependence for parameters such as the zero-pressure volume (V_0), the zero-pressure bulk modulus (K_0), and its pressure derivative (K'_0).

Before comparing with experimental data, it is essential to define the theoretical setup most likely to produce accurate predictions of equilibrium isotope fractionation. In cases where direct experimental data is unavailable, we consider the combination of the PBESOL exchange–correlation functional, explicit thermal expansion treatment, and averaging across the two distinct Mg sites in forsterite as the most physically sound and consistent methodological approach. This setup offers the best overall representation of the structural and vibrational properties in silicate minerals and is thus used as the reference model for further analysis.

3. Results

3.1 Experimental run products

Table 2, Experimental run conditions, phase proportions and compositions of runs analysed for their isotopic compositions.

Experiment	Phase	T (K)	Duration (days)	Phase proportions (wt%)	n[a]	MgO	SiO_2	Al_2O_3	CaO	Total	n[a]	$\delta^{26}Mg$	2 s.e.

S2-1(Di)		1573	7	Glass (64), Di (36)									
	melt				10	11.61 (5)	49.11 (3.7)	17.47 (9)	22.21 (2.6)	100.41	12	-1.372	0.023
	diopside				14	17.62 (2.7)	52.93 (3.6)	5.27 (8.1)	25.01 (2.1)	100.83	12	-1.312	0.023
S1-4 (Fo)		1560	7	Glass (80), Di (20)									
	melt				10	13.86 (0.9)	48.72 (2.3)	15.7 (0.7)	21.62 (0.6)	99.9	36	-1.362	0.018
	forsterite				20	56.95 (2.4)	42.7 (1.3)	0.08 (0.1)	0.68 (0.1)	100.42	18	-1.42	0.025

[a] Compositions are given as the averages of *n* analyses. [b] Mass fraction phase proportions obtained by mass-balance calculations. Major element compositions reported as weight percentages with uncertainties given in parentheses as 10^{-1} (s.e).

We selected the two beads with the biggest crystals for isotope analysis: BDW-S2-1 (Di), comprising diopside crystals with diameters ≥ 400 µm, and BDW-S1-4 (Fo), containing forsterite crystals with diameters ≥ 250 µm (Figure 2). Several additional experimental charges were created during this study; however, most produced crystals too small for reliable microdrilling or isotope analysis, leaving only two charges suitable for determining equilibrium fractionation factors. A representative backscattered electron image (BSE) of a polished cross-section is shown in Figure 2. Neither the melt nor the mineral phases show any heterogeneity, despite the skeletal textures of the diopside crystals (Table 2 and Supplementary Figures S1-1, S1-2). Mass balance calculations reveal that the mineral phases comprise 19.57 wt% for S1 (Fo) and 36.56 wt% for S2 (Di), within 1 wt% of the proportions expected by applying the lever rule to the phase diagram shown in Figure 1.

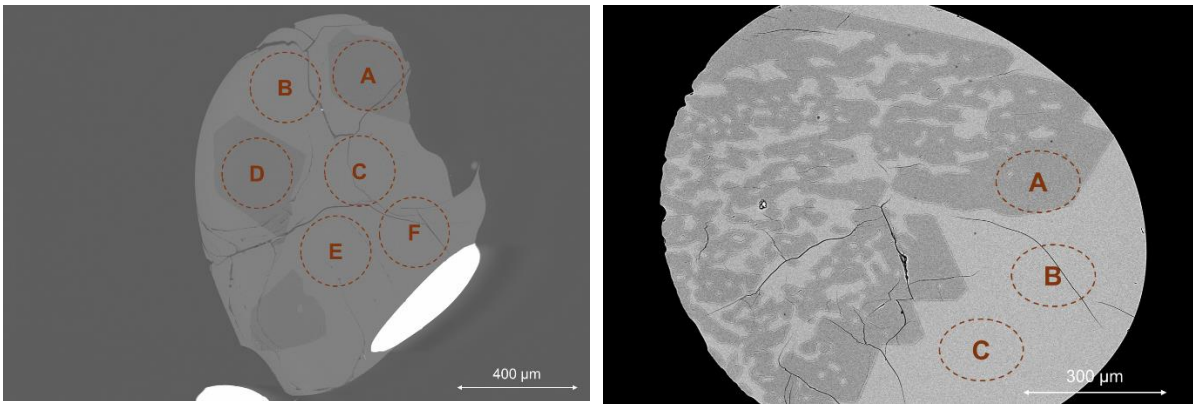

BDW-S1-4 (Fo) BDW-S2-1 (Di)

Figure 2, BSE images of experimental run products: a) bead BDW-S1-4 containing three Fo crystals and b) bead BDW-S2-1 containing a large Di crystal. These beads were used for micro drilling and isotope analysis. Orange dotted circles show the drill sites with letters corresponding to isotope samples reported in Supplementary Table S1-1.

3.2 Experimental isotope analysis

Liu et al. (2022) observed that, in the experimental materials, the isotope ratio varied systematically with position within experimental charges that experience significant temperature differences, suggesting the occurrence of the Soret diffusion, making the experimental runs less reliable for providing convincing isotope fractionation factors. In contrast, our measurements (Supplementary Table S1-1) show nice homogeneity (2 s.e. = ± 0.025‰, comparable to the analytical precision limit of ± 0.027‰, Liu et al., 2023) across multiple sites within a single sample, in contrast to the up to 0.6 ‰ δ^{26}Mg variance seen in Liu et al. (2022). Therefore, we believe our samples do not exhibit thermal gradients or the Soret effect under the current analytical precision.

We drilled out a total of six melt samples across the beads (Figure 2, orange dotted circles). Individual measurements of drill sites are given in Supplementary Table S1-1. The average Mg isotope composition for each phase in each bead is reported in Table 2. Average Δ^{26}Mg for ol-melt and cpx-melt are $\Delta^{26}Mg_{ol/melt}$ = -0.058 ± 0.032 at 1573 ± 2.5 K and $\Delta^{26}Mg_{cpx/melt}$ = 0.060 ± 0.034 at 1560 ± 2.5 K. Assuming this fractionation varies as $1/T^2$ (where T is temperature in K) and tends to zero as the temperature tends to infinity (expected for equilibrium fractionation: Urey, 1947)) results in $\Delta^{26}Mg_{cpx/melt} = (1.49 \pm 0.84) \times 10^5/T^2$ and $\Delta^{26}Mg_{ol/melt} = (-1.44 \pm 0.79) \times 10^5/T^2$ (Fig. 3a&b). Our $\Delta^{26}Mg_{ol/melt}$ value is in good consistence with previous reported $\Delta^{26}Mg_{ol/melt}$ value obtained from naturally quenched olivine-glass pairs (Liu et al., 2022) (Fig. 3a). Furthermore, based on these obtained $\Delta^{26}Mg_{ol/melt}$ and $\Delta^{26}Mg_{cpx/melt}$ values, we can then

315 have a $\Delta^{26}Mg_{cpx/ol} = 0.118 \pm 0.045$ at an average temperature of 1566.5 ± 6 K, and yielding

316 $\Delta^{26}Mg_{cpx/ol} = (2.93 \pm 1.15) \times 10^5/T^2$ (Fig. 3c).

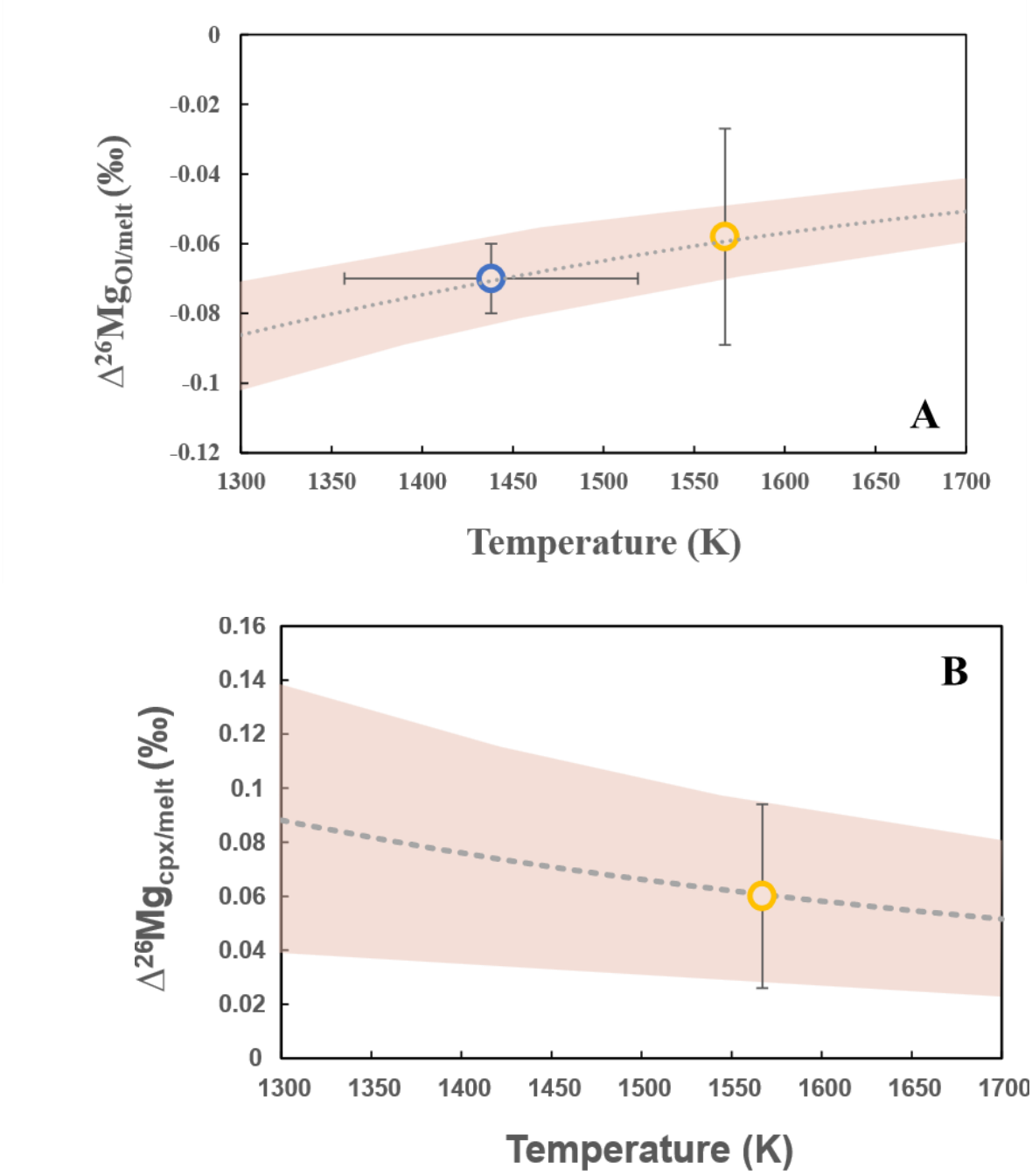

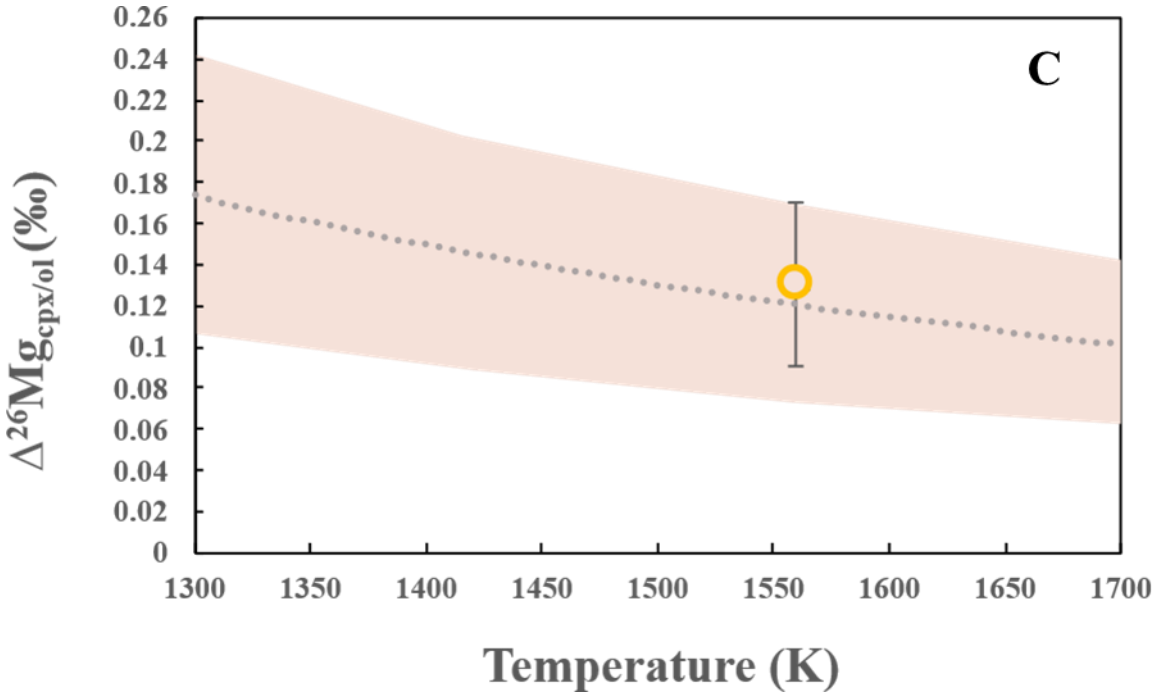

Figure 3, Mg isotopic difference between: (a) olivine-melt plotted against temperature for this study (yellow symbol) and compared with data from Liu et al. 2022 (blue symbol). Temperature uncertainties in experiments are expected to be < 2.5 K (°C) and therefore not plotted as error bars. Dashed line represents the estimated $\Delta^{26}Mg_{ol/melt}$ as a function of temperature from Liu et al. (2022). (b) clinopyroxene-melt plotted against temperature with $\Delta^{26}Mg_{cpx/melt}$ calculated in this study. (c) clinopyroxene-olivine plotted against temperature.

3.3 Ab initio calculations

First, we evaluate the influence of the chosen exchange-correlation functionals on the mineral structures of diopside and forsterite. Our calculations were conducted using the LDA, GGA, and PBESOL exchange-correlation functionals. Results following geometry optimisation show that the calculated cell parameters (Table S2-2) and the Mg-O bond lengths (Table S2-1) for the PBESOL functional are much closer to experimental values than those obtained with LDA or PBE functionals (Figure 4).

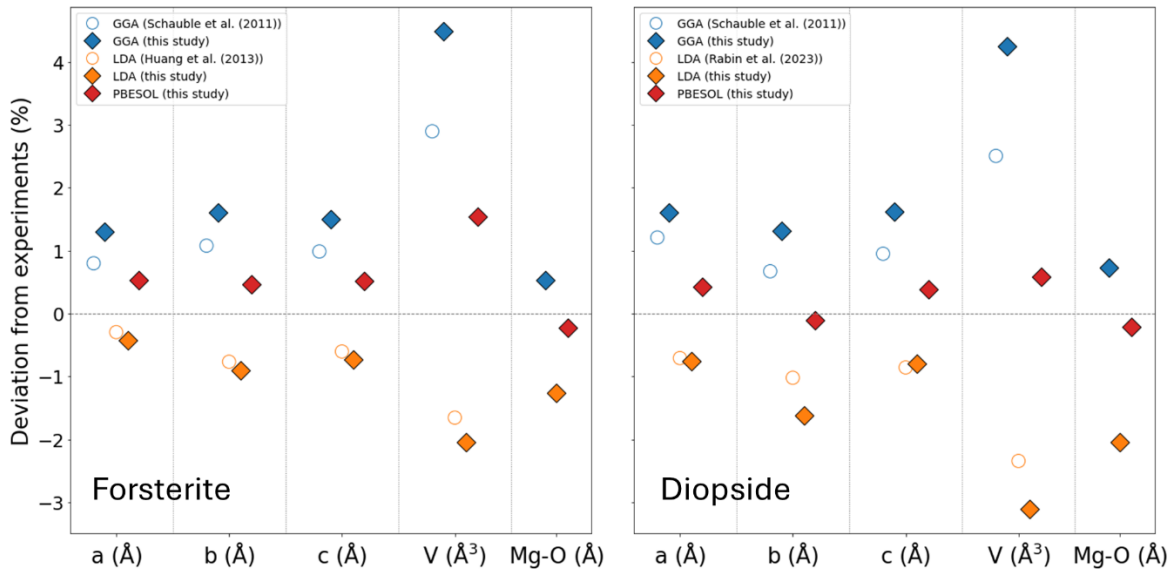

Figure 4, Deviation of calculated cell parameters and Mg–O bond lengths (Supplementary Table S2-2) from experimentally determined crystal structures, with static (0 K) DFT results compared to experimental studies at the lowest temperature found. Diopside at 10 K (Prencipe et al., 2000), forsterite at 77 K (Hazen, 1976). PBESOL shows the smallest deviation across all metrics, indicating better agreement with the experimental crystal structure.

Supplementary Figure S2-1 illustrates the temperature dependence of the averaged reduced partition function (ß) of forsterite and diopside using E_{xc} PBESOL, LDA and PBE compared to previous studies. (Huang et al., 2013; Schauble, 2011; Wang et al., 2023). An overview of the methodologies used in the literature is given in Supplementary Table 2-3. The polynomial fit parameters of the ß-values calculated in this study are detailed in Table 3.

It is important to understand how the choice of exchange–correlation functional affects the relative reduced partition functions that enter isotope fractionation factors, and to distinguish this effect from differences that arise solely from changes in the calculated crystal structure. To explore this, we conducted additional calculations using the PBESOL, PBE, and LDA exchange-correlation functionals for forsterite while fixing the unit cell volume to its experimental value. First, we used fixed-volume calculations for forsterite and observed

differences in ß(^{26}Mg/^{24}Mg) of 0.04 ‰ (LDA) and -0.02 ‰ (PBE) relative to PBESOL. To assess how structural differences influence isotope fractionation independently of the exchange–correlation functional, we conducted PBESOL calculations to examine the effect of variations in Mg–O bond lengths on the reduced partition function. Small bond length changes were induced by applying different external pressures, which systematically altered the unit-cell volume while maintaining a fixed functional. These calculations revealed a Mg isotope fractionation sensitivity of 0.00375‰ for every 0.001 Å change in Mg–O bond length. Using the sensitivity of Mg isotope fractionation to Mg–O bond length derived from the PBESOL pressure-dependent calculations, and the differences in average Mg–O bond length between the fixed-volume PBESOL, LDA, and PBE structures (Supplementary Table S2-1), we estimate that only ~0.003‰ (LDA) and ~0.0006‰ (PBE) of the total offset can be attributed to bond length differences. The remaining offsets, therefore, arise from the direct effect of the exchange–correlation functional force constants.

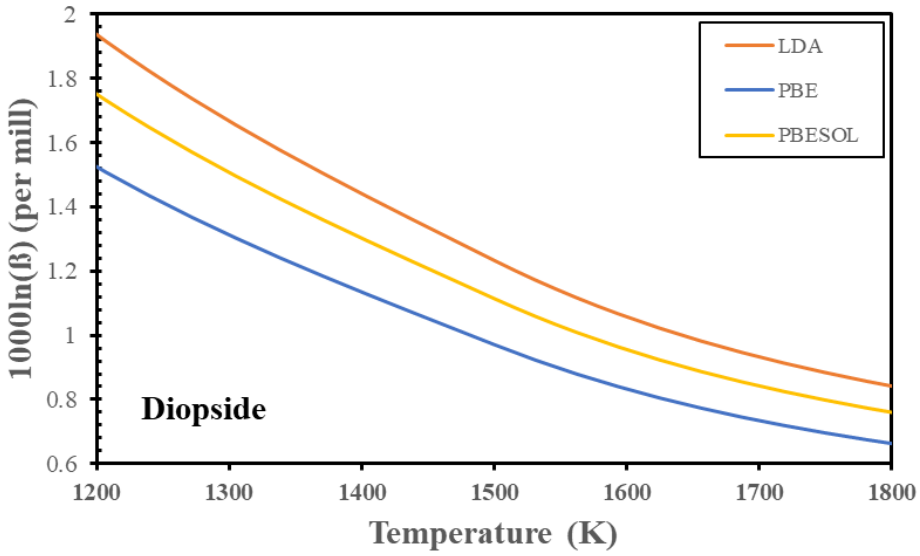

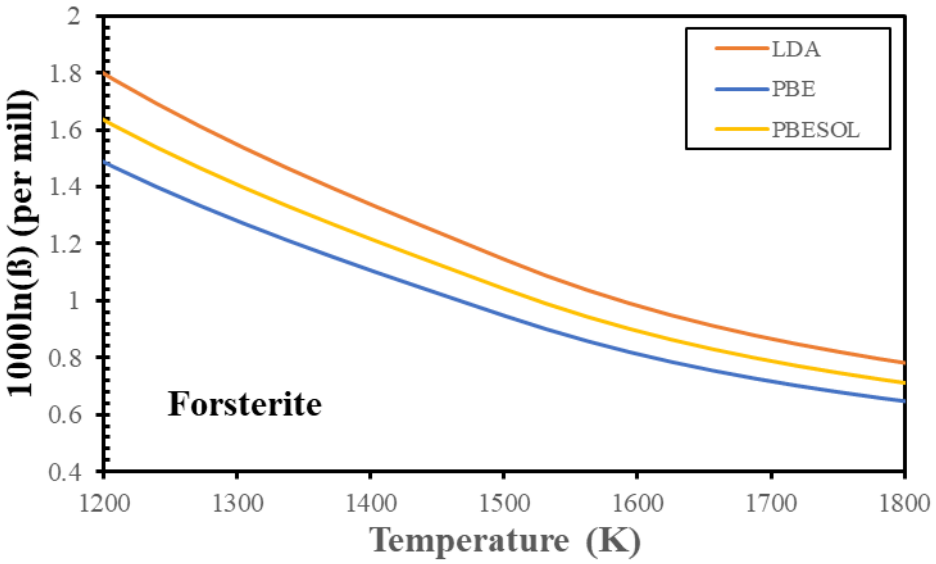

Figure 5, Reduced partitioning function for magnesium isotopes in a) diopside and b) Forsterite.

	A	B	C
Forsterite PBESOL M1	2.809×10^{14}	-1.766×10^{10}	2.523×10^{6}
Forsterite PBESOL Average	*2.613×10^{14}*	*-1.642×10^{10}*	*2.346×10^{6}*
Forsterite PBESOL M2	2.416×10^{14}	-1.519×10^{10}	2.170×10^{6}
Forsterite PBE	2.325×10^{14}	-1.464×10^{10}	2.134×10^{6}
Forsterite LDA	2.447×10^{14}	-1.541×10^{10}	2.247×10^{6}
Diopside PBESOL	2.163×10^{14}	-1.565×10^{10}	2.518×10^{6}
Diopside PBE	1.535×10^{14}	-1.218×10^{10}	2.188×10^{6}
Diopside LDA	2.720×10^{14}	-1.880×10^{10}	2.783×10^{6}

Table 3. Polynomial fitted constants for 1000 ln (ß (X, ^{24}Mg, ^{26}Mg) = $AT^{-6}+BT^{-4}+CT^{-2}$ as a function of T in Kelvin from 1000-4000 K.

348 Here, we approach the different cation sites in forsterite, similar to Duan et al. (2023), where
349 we calculate the M1 and M2 sites and average them to produce a single 10^3 lnβ for δ^{26}Mg in
350 forsterite (Figure 6). We observe a 14% difference in 10^3 lnβ for δ^{26}Mg between the M1 and
351 M2 sites. Diopside has only one cation site for Mg, so it does not require averaging.

352 Lastly, recent studies have shown the impact of thermal expansion on phonon frequencies and,
353 consequently, on isotope fractionation. (Walker et al., 2025; Wang et al., 2023). Our calculated

temperature dependent third-order Birch-Murnaghan parameters were fitted to fifth-order polynomials (Supplementary S2-4). These were then used to evaluate cell volume as a function of temperature and pressure. In addition, we calculated ß as a function of temperature. We fitted this to a polynomial in volume and temperature (Supplementary table S2-5). Figure 6 illustrates the 10^3 lnβ for $\delta^{26}Mg$ for Fo and Di, accounting for thermal expansion. The correction for thermal expansion is significant, as this slight change in unit-cell parameters leads to larger differences in $\Delta^{26}Mg_{cpx/ol}$ values. Our thermal expansion corrections yield average the thermal expansivity coefficients calculated for forsterite, $\alpha = 4.92 \times 10^{-5}$ K^{-1}; for diopside, $\alpha = 2.50 \times 10^{-5}$ K^{-1}. These values are consistent with those found in previous experimental studies (Bouhifd et al., 1996; Finger & Ohashi, 1976). In contrast, the *ab initio* study of Wang et al. (2023) reported that diopside ($\alpha = 7.22 \times 10^{-5}$ K^{-1}) expands more than forsterite ($\alpha = 6.44 \times 10^{-5}$ K^{-1}), which leads to opposite effects in their $\Delta^{26}Mg_{cpx/ol}$ calculations using different exchange-correlation functionals (LDA). This discrepancy highlights how the choice of exchange functional and the thermal expansion correction significantly influence the accuracy of isotope fractionation predictions.

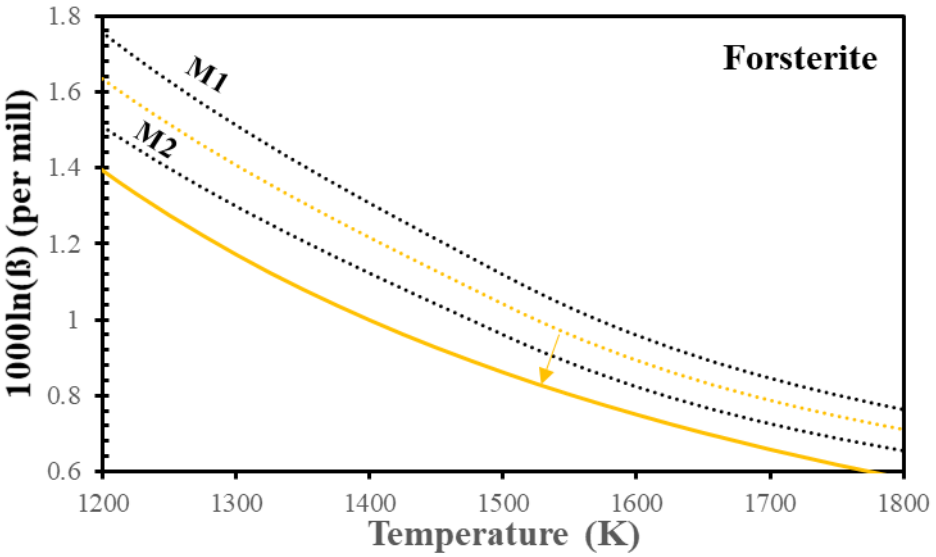

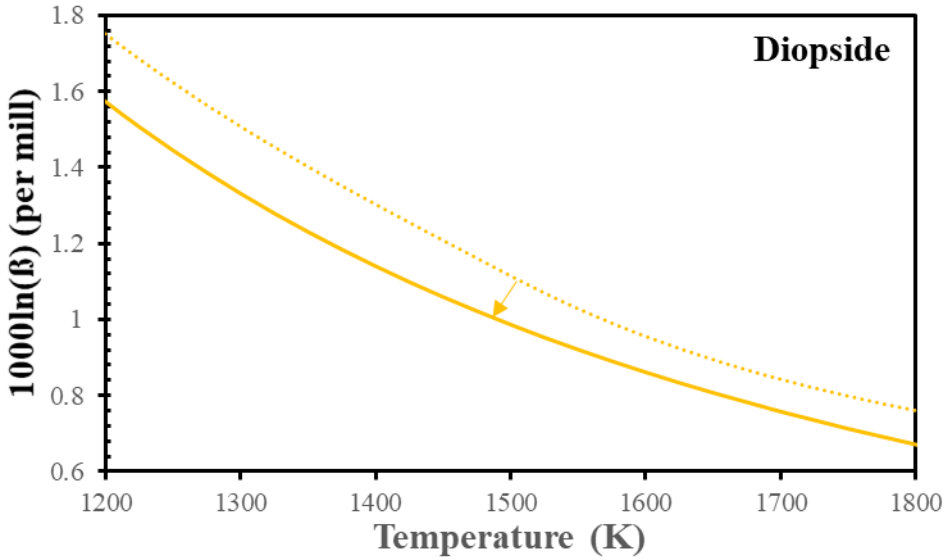

Figure 6, Reduced partitioning function with thermal expansion correction (yellow solid line) and without thermal expansion (yellow dotted line). The M1 and M2 sites (black dotted line) are averaged and then corrected for thermal expansion.

	Fo	Di
A_1 (K^6)	-1.5252×10^{15}	-9.4405×10^{14}
A_2 ($K^6Å^3$)	5.2452×10^{17}	5.1513×10^{17}
B_1 (K^4)	-1.2555×10^{11}	-2.8136×10^{11}
B_2 ($K^4Å^3$)	9.1326×10^{13}	2.7616×10^{14}
B_3 ($K^4Å^6$)	-1.7484×10^{16}	-7.0174×10^{16}
C_1 (K^2)	1.1904×10^{6}	9.5665×10^{6}
C_2 ($K^2Å^3$)	-1.3578×10^{9}	-9.7941×10^{9}
C_3 ($K^2Å^6$)	5.0313×10^{11}	2.9521×10^{12}

Table 4, Coefficients of the polynomial $1000 \ln(\beta(V, T)) = (A_1 + A_2V^{-1}) T^{-6} + (B_1 + B_2V^{-1} + B_3V^{-2}) T^{-4} + (C_1 + C_2V^{-1} + C_3V^{-2}) T^{-2}$ to calculate the reduced partition functions with thermal expansion correction between 300-1900 K with respective cell volumes.

3.4 Comparison between experimental and theoretical results.

We demonstrate a good agreement between the $\Delta^{26}Mg_{cpx/ol}$ ratios obtained from our experiments and those predicted by our PBESOL *ab initio* calculations performed with thermal

expansion correction (Figure 7). The experimentally determined $\Delta^{26}Mg_{cpx/ol}$ ratios offer a reference point to evaluate the impacts of various exchange-correlation functionals, site averaging, and thermal expansion treatments on calculated equilibrium isotope fractionation. Notably, the calculated isotope fractionation ratios utilising the PBESOL functional with thermal expansion correction fall within the uncertainty range of the measured $\Delta^{26}Mg_{cpx/ol}$ values (Fig 7). In contrast, calculations based on other exchange–correlation functionals, including LDA (Huang et al., 2013), LDA + QHA (Wang et al., 2023), and GGA (Schauble, 2011), yield $\Delta^{26}Mg_{cpx/ol}$ values that are lower than our experimentally constrained value by ~0.02‰ at 1573 K. These studies do not explicitly account for thermal expansion in the calculation of inter-mineral fractionation factors. Our results show that thermal expansion introduces a correction due to the reduced partition functions of olivine being relatively larger compared to diopside, suggesting that neglecting this effect is likely to contribute substantially to the apparent offset between these calculations and experimental constraints.

Interestingly, the calculations performed by Schauble et al. (2011) using GGA as E_{xc} do not agree with our GGA (PBE) calculations. The variations between our calculations and Schauble et al. (2011) reflect instead a difference in approach to translating phonon frequencies to reduced partition function ratios (ß). Previously, it was a common approach to use a scale factor to correct vibrational frequencies for softening in the functional group when comparing results with those from vibrational spectroscopy (Schauble, 2011). More recent work (Huang et al., 2013; Walker et al., 2025; Young et al., 2015) shows that computational methods have improved, and uniform scaling is physically simplistic; first-principles predictive accuracy can be reached (e.g., PBESOL) without empirical tuning.

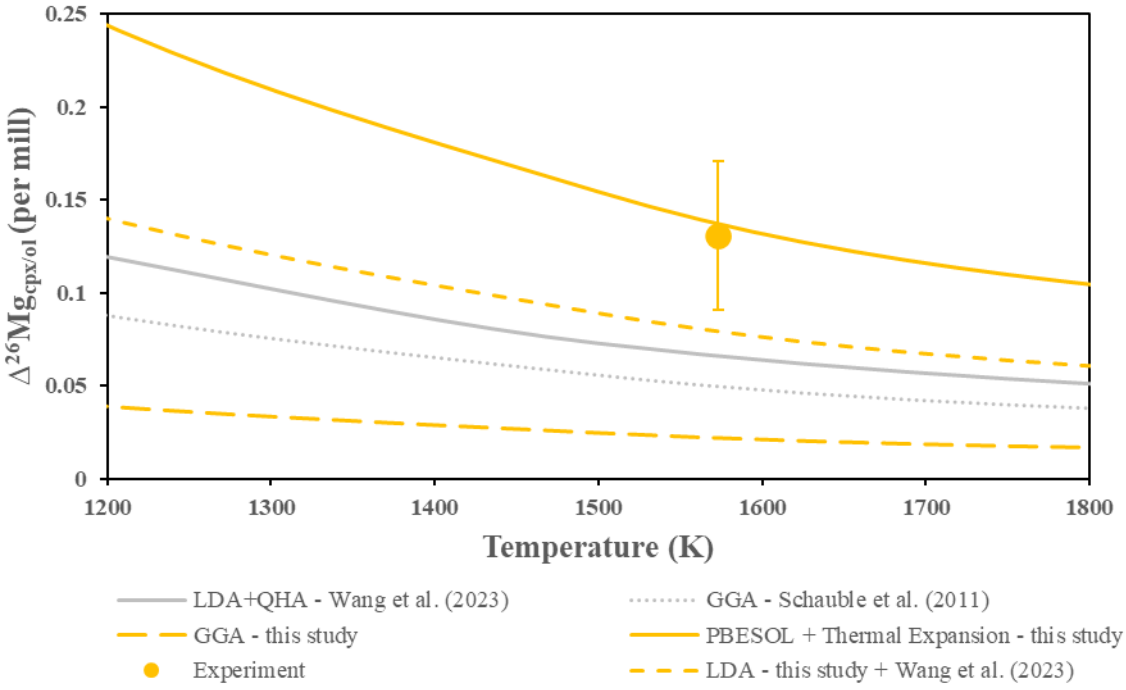

Figure 7, Inter-mineral Mg isotope fractionation between diopside and forsterite plotted as a function of temperature and compared with density functional theory calculations at 0 GPa from this study and from the literature. Static-volume calculations using GGA/PBE (yellow striped) and LDA (yellow dotted) are shown. LDA results from this study and from Wang et al. (2023) overlap within the resolution of the figure and are therefore represented by the same symbol.

4. Discussion

Our results show good agreement between experimental determination of a value of $\Delta^{26}Mg_{cpx/ol}$ and its DFT Mg calculation (Fig.7). The PBESOL functional, when combined with thermal expansion and site averaging in forsterite, reproduces the measured $\Delta^{26}Mg_{cpx/ol}$ values most accurately, suggesting that this approach provides the most reliable basis for modelling equilibrium isotope behaviour in silicate minerals. In comparison, LDA and PBE underestimate Mg isotope fractionation in diopside and forsterite.

4.1 Comparison with literature data for Mg isotopic fractionation between olivine and clinopyroxene in naturally occurring samples

Previous studies (e.g Chen et al., 2018; Hu et al., 2020; X. Liu et al., 2022; X.-N. Liu et al., 2023; Pogge von Strandmann et al., 2011; Stracke et al., 2018; Yang et al., 2009) have investigated magnesium isotopic fractionation across various mineral phases in natural samples. $\Delta^{26}Mg_{cpx/ol}$ from most studies relying on sample–standard bracketing exhibit significant analytical uncertainties (> ±0.1‰, 2sd; Supplementary Table S1-3) and are therefore not well suited for quantitative testing of ab initio predictions. Nevertheless, despite their limited precision, such measurements have consistently shown fractionation factors of the same sign and order of magnitude as those predicted by atomic-scale simulations (e.g. Stracke et al., 2018; Young et al., 2009). The recent dataset from Liu et al. (2022 & 2023), which employs a critical mixture double-spiking method, provides a higher precision benchmark against which our experimental findings can be compared (Figure 8). While our measurements show a $\Delta^{26}Mg_{cpx/ol}$ value that closely matches Liu et al. (2023), who reported 0.131 ± 0.045‰, our experimental temperature is roughly 300 K higher than the temperatures estimated for their natural samples. Our theoretical calculations of equilibrium fractionation predict that at temperatures around 1300 K, we would expect the $\Delta^{26}Mg_{cpx/ol}$ values to be approximately 0.2‰ higher between the diopside-olivine phases. This suggests that other processes influence isotope ratios beyond equilibrium isotope fractionation.

This conclusion is further supported when the data are evaluated using relative olvine-clinopyroxene Mg#. We calculated the relative Mg# differences between coexisting olvine and clinopyroxene in the samples used by Liu et al. (2023), following Sen (1988). Most samples exhibit small Mg# differences, usually within ±0.5 Mg#, suggesting near-equilibrium Fe-Mg partitioning between olivine and cpx. A smaller group of samples shows slight positive offsets, with olivine containing more Mg than cpx, up to +2 Mg#. Importantly, however, even samples that show near-equilibrium Fe-Mg partitioning yield $\Delta^{26}Mg_{cpx/ol}$ values that are systematically lower than our experimentally determined equilibrium fractionation. This indicates that

agreement in Fe-Mg exchange does not guarantee equilibrium Mg-isotope fractionation and suggests that kinetic effects or incomplete isotopic equilibrium may persist in natural systems even where major-element partitioning appears equilibrated.

Minor but systematic deviations from equilibrium Mg isotope fractionation may arise during xenolith ascent, when decreasing temperature shifts the equilibrium Fe-Mg partitioning between olivine and clinopyroxene. Experimental and thermodynamic studies show that cooling favors an increase in Mg# of clinopyroxene relative to olivine, driving Mg diffusion from olivine into clinopyroxene as the system attempts to re-equilibrate (Putirka, 2008; Sen, 1988). Because Mg diffusion is faster than complete Fe-Mg re-equilibration, this process may halt before equilibrium is fully achieved. Diffusion-driven isotope fractionation then results in isotopically light Mg being concentrated in clinopyroxene rims, while olivine rims become relatively heavy, leading to a net reduction in $\Delta^{26}Mg_{cpx/ol}$ compared to the high-temperature equilibrium value. Such kinetic isotope effects during mineral diffusion are well documented in a range of mineral systems (Oeser et al., 2015; Richter et al., 2009; Sio et al., 2013). However, the effect in Hawaiian xenoliths studied by Liu et al. (2023) is likely limited, since these samples erupted explosively and cooled quickly, reducing the time for post-entrapment diffusion. The small $\Delta^{26}Mg_{cpx/ol}$ values and lack of major-element disequilibrium in mineral cores indicate that Fe–Mg re-equilibration was minimal, and that diffusive changes mostly dampened, rather than overprinted, the original Mg isotope signatures.

Alternatively, differences in $\Delta^{26}Mg_{cpx/ol}$ between natural and experimental mineral pairs could reflect the simplified, iron-free nature of the experimental system. However, our results show that both $\Delta^{26}Mg_{ol/melt}$ and $\Delta^{26}Mg_{cpx/melt}$ determined in this iron-free system are consistent, within uncertainty, with values from natural, Fe-bearing samples (Liu et al., 2022; Liu et al., 2023). This suggests that iron content does not exert a first-order control on equilibrium Mg isotope fractionation between mineral phases and melt and therefore is unlikely to dominate olvine-

clinopyroxene fractionation either. While theoretical frameworks have proposed that cation electronegativity and bonding environment may influence isotope fractionation (Méheut & Schauble, 2014), direct experimental constraints on the effect of iron on Mg isotope fractionation remain limited. Further experiments incorporating iron would nonetheless be valuable for testing for any subtle or second-order effects beyond the scope of this study.

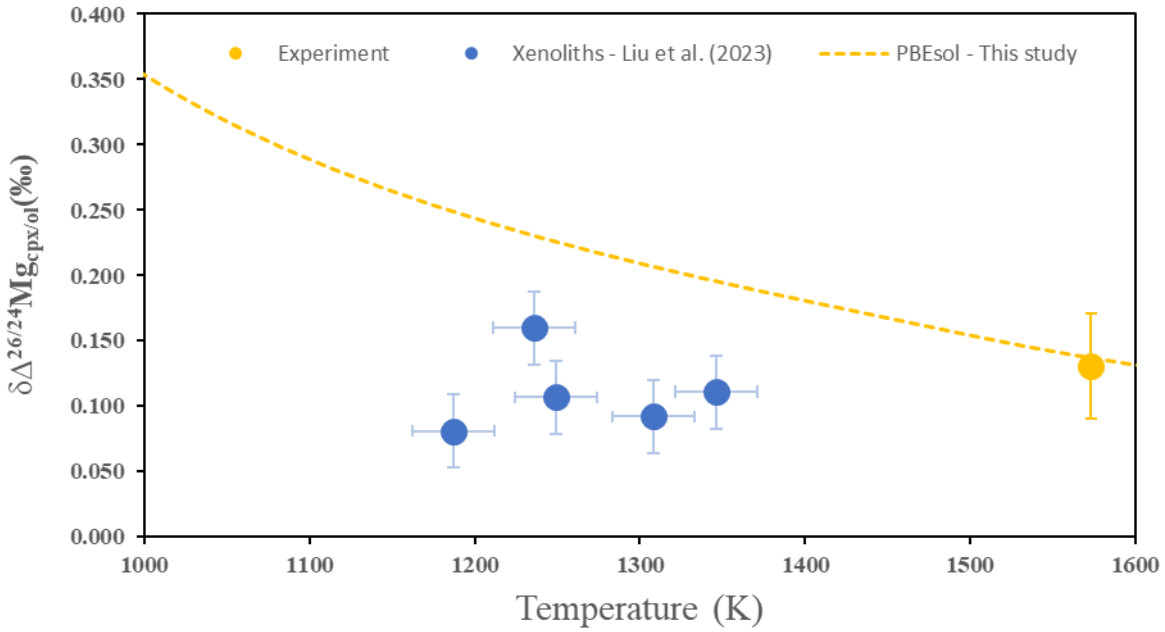

Figure 8, Inter-mineral Mg isotopic differences for clinopyroxene-olivine with PBESOL + site averaging + thermal expansion (tallow line) plotted against temperature in Kelvin and compared to xenoliths from Liu et al. (2023)

4.2 Constraints on $\Delta^{26}Mg_{ol/melt}$ from experiments.

Unlike the $\Delta^{26}Mg_{cpx/ol}$, our $\Delta^{26}Mg_{ol/melt}$ matches the ratio reported by Liu et al. (2022) (Figure 3a). Although the compositions of residual melts and mineral phases in our experiments differ from those in the natural samples analysed by Liu et al., our results are complementary and consistent with the observed $\Delta^{26}Mg_{ol/melt} = (-1.46 \pm 0.26) \times 10^5/T^2$. This contrasts with the assumption of $\Delta^{26}Mg_{ol/melt} = 0$ (e.g. Soderman et al., 2024; Stracke et al., 2018) based on the work of Teng et al. (2007). The difficulty of accounting for the $\delta^{26}Mg$ of many mantle-derived basalts using equilibrium melting processes with the olivine-melt fractionation factor of Liu et

al. (2022) led Soderman et al. (2024) to argue for the continued use of $\Delta^{26}Mg_{ol/melt} = 0$. That our new experimental results strongly support the $\Delta^{26}Mg_{ol/melt}$ reported by Liu et al (2022), this emphasises the need to consider diffusive fractionation during magma migration to the surface in shaping erupted $\delta^{26}Mg$ (and $\delta^{57}Fe$) of mantle-derived melts (Liu et al., 2024).

Future research should focus on refining mineral–melt Mg isotope fractionation factors by expanding high-temperature experimental datasets to include a wider range of melt compositions, pressures, and redox conditions. Additionally, better constraints on the isotopic equilibrium between crystals and coexisting melts are needed. Specifically, systematic experiments that isolate compositional effects- such as melt polymerisation and Mg coordination, and exclude kinetic overprints are important for enhancing the accuracy of mineral–melt fractionation factors and precise modelling of Mg isotope fractionation during large-scale differentiation in larger planetary bodies, where the pressure–temperature conditions and crystallisation timescales substantially differ from those studied in this research.

5. Conclusions

In this study, we assess the magnitude of Mg equilibrium isotope fractionation between forsterite and diopside at liquidus temperatures, using both data from petrological experiments and theoretical calculations. Our measurements of $\Delta^{26}Mg_{ol/melt}$ = -0.058 ± 0.032 and $\Delta^{26}Mg_{cpx/melt}$ = 0.060 ± 0.034 at 1300 °C / 1573 K allow us to calculate the first experimentally derived isotope fractionation factor for this mineral pair, with $\Delta^{26}Mg_{cpx/ol}$ = 0.131 ± 0.04 at 1576 K.

Our findings align well with ab initio calculations based on density functional theory (DFT), particularly emphasising the effectiveness of the PBESOL exchange-correlation functional and the thermal expansion correction in accurately modelling the $\Delta^{26}Mg_{cpx/ol}$ ratio. These consistent

493 constraints emphasise the value of precise computational methods and experimentally obtained
494 fractionation factors by producing a single, experimentally anchored $\Delta^{26}Mg_{cpx/ol}$ ratio.

495 Acknowledgements

496 We thank Krzystof Sokol and Andrew Matzen for their assistance with electron microscopy at
497 the University of Oxford, and Chris Coath for his help in analysing isotopic data at the
498 University of Bristol. This research was funded by ERC Advanced Grant 883351 NONUNE
499 to TE and BdW received financial support through an Oxford Radcliffe Scholarship from
500 University College, Oxford. For the purpose of Open Access, the authors have applied a CC
501 BY public copyright licence to any Author Accepted Manuscript (AAM) version arising from
502 this submission. The authors would like to acknowledge the use of the University of Oxford
503 Advanced Research Computing (ARC) facility and the ARCHER2 UK National
504 Supercomputing Service (https://www.archer2.ac.uk) in carrying out this work.

505 Data availability

506 Density functional theory calculations were performed using the CASTEP code, available via
507 https://www.castep.org/. Input and output files for these calculations are available through
508 Zenodo via https://doi.org/10.5281/zenodo.18195898.

509 Appendix A. Supplementary Material

510 The supplementary material provides further details on the experiments and ab initio
511 calculations employed in this study.

512 References

513 Blanchard, M., Balan, E., & Schauble, E. A. (2017). Equilibrium Fractionation of Non-
514 traditional Isotopes: A Molecular Modeling Perspective. *Reviews in Mineralogy and*
515 *Geochemistry*, *82*(1), 27–63. https://doi.org/10.2138/rmg.2017.82.2
516 Blanchard, M., Poitrasson, F., Méheut, M., Lazzeri, M., Mauri, F., & Balan, E. (2009). Iron
517 isotope fractionation between pyrite (FeS2), hematite (Fe2O3) and siderite (FeCO3): A
518 first-principles density functional theory study. *Geochimica et Cosmochimica Acta*,
519 *73*(21), 6565–6578. https://doi.org/10.1016/j.gca.2009.07.034
520 Bouhifd, M. A., Andrault, D., Fiquet, G., & Richet, P. (1996). Thermal expansion of forsterite
521 up to the melting point. *Geophysical Research Letters*, *23*(10), 1143–1146.
522 https://doi.org/10.1029/96GL01118
523 Chen, H.-W., Claydon, J. L., Elliott, T., Coath, C. D., Lai, Y.-J., & Russell, S. S. (2018).
524 Chronology of formation of early solar system solids from bulk Mg isotope analyses of
525 CV3 chondrules. *Geochimica et Cosmochimica Acta*, *227*, 19–37.
526 https://doi.org/10.1016/j.gca.2018.02.011
527 Clark, S. J., Segall, M. D., Pickard, C. J., Hasnip, P. J., Probert, M. I. J., Refson, K., & Payne,
528 M. C. (2005). First principles methods using CASTEP. *Zeitschrift Für Kristallographie*
529 *- Crystalline Materials*, *220*(5–6), 567–570.
530 https://doi.org/10.1524/zkri.220.5.567.65075
531 Coath, C. D., Elliott, T., & Hin, R. C. (2017). Double-spike inversion for three-isotope systems.
532 *Chemical Geology*, *451*, 78–89. https://doi.org/10.1016/j.chemgeo.2016.12.025
533 Downs, R. T., & Hall-Wallace, M. (2003). The American Mineralogist crystal structure
534 database. *American Mineralogist*, *88*(1), 247–250.
535 Duan, H., Yang, B., & Huang, F. (2023). Site-specific isotope effect: Insights from equilibrium
536 magnesium isotope fractionation in mantle minerals. *Geochimica et Cosmochimica*
537 *Acta*. https://doi.org/10.1016/j.gca.2023.05.014

538 Finger, L. W., & Ohashi, Y. (1976). The thermal expansion of diopside to 800 degrees C and
539 a refinement of the crystal structure at 700 degrees C. *American Mineralogist*, *61*(3–4),
540 303–310.
541 Giannozzi, P., de Gironcoli, S., Pavone, P., & Baroni, S. (1991). Ab initio calculation of phonon
542 dispersions in semiconductors. *Physical Review B*, *43*(9), 7231–7242.
543 https://doi.org/10.1103/PhysRevB.43.7231
544 Gonze, X. (1997). First-principles responses of solids to atomic displacements and
545 homogeneous electric fields: Implementation of a conjugate-gradient algorithm.
546 *Physical Review B*, *55*(16), 10337–10354. https://doi.org/10.1103/PhysRevB.55.10337
547 Gonze, X., & Lee, C. (1997). Dynamical matrices, Born effective charges, dielectric
548 permittivity tensors, and interatomic force constants from density-functional
549 perturbation theory. *Physical Review B*, *55*(16), 10355–10368.
550 https://doi.org/10.1103/PhysRevB.55.10355
551 Hazen, R. M. (1976). Effects of temperature and pressure on the crystal structure of forsterite.
552 *American Mineralogist*, *61*(11–12), 1280–1293.
553 He, Y., Sun, A.-Y., Zhang, Y.-C., Yang, R.-Y., Ke, S., Wang, Y., & Teng, F.-Z. (2022). High-
554 precision and high-accuracy magnesium isotope analysis on multiple-collector
555 inductively coupled plasma mass spectrometry using a critical mixture double spike
556 technique. *Solid Earth Sciences*, *7*(3), 188–199.
557 https://doi.org/10.1016/j.sesci.2022.05.001
558 Hin, R. C., Coath, C. D., Carter, P. J., Nimmo, F., Lai, Y. J., Pogge von Strandmann, P. A. E.,
559 Willbold, M., Leinhardt, Z. M., Walter, M. J., & Elliott, T. (2017). Magnesium isotope
560 evidence that accretional vapour loss shapes planetary compositions. *Nature*,
561 *549*(7673), 511–527. https://doi.org/10.1038/nature23899

562 Hohenberg, P., & Kohn, W. (1964). Inhomogeneous electron gas. *Physical Review*, *136*(3B),
563 B864. https://doi.org/10.1103/PHYSREV.136.B864/FIGURE/1/THUMB
564 Hu, Y., Teng, F.-Z., & Ionov, D. A. (2020). Magnesium isotopic composition of metasomatized
565 upper sub-arc mantle and its implications to Mg cycling in subduction zones.
566 *Geochimica et Cosmochimica Acta*, *278*, 219–234.
567 https://doi.org/10.1016/j.gca.2019.09.030
568 Huang, F., Chen, L., Wu, Z., & Wang, W. (2013). First-principles calculations of equilibrium
569 Mg isotope fractionations between garnet, clinopyroxene, orthopyroxene, and olivine:
570 Implications for Mg isotope thermometry. *Earth and Planetary Science Letters*, *367*,
571 61–70. https://doi.org/10.1016/j.epsl.2013.02.025
572 Javoy, M., Balan, E., Méheut, M., Blanchard, M., & Lazzeri, M. (2012). First-principles
573 investigation of equilibrium isotopic fractionation of O- and Si-isotopes between
574 refractory solids and gases in the solar nebula. *Earth and Planetary Science Letters*,
575 *319–320*, 118–127. https://doi.org/10.1016/j.epsl.2011.12.029
576 Kieffer, S. W. (1982). Thermodynamics and lattice vibrations of minerals: 5. Applications to
577 phase equilibria, isotopic fractionation, and high-pressure thermodynamic properties.
578 *Reviews of Geophysics*, *20*(4), 827–849. https://doi.org/10.1029/RG020i004p00827
579 Kohn, W., & Sham, L. J. (1965). Self-Consistent Equations Including Exchange and
580 Correlation Effects. *Physical Review*, *140*(4A), A1133–A1138.
581 https://doi.org/10.1103/PhysRev.140.A1133
582 Lai, Y.-J., Pogge von Strandmann, P. A. E., Dohmen, R., Takazawa, E., & Elliott, T. (2015).
583 The influence of melt infiltration on the Li and Mg isotopic composition of the
584 Horoman Peridotite Massif. *Geochimica et Cosmochimica Acta*, *164*, 318–332.
585 https://doi.org/10.1016/j.gca.2015.05.006

586 Li, X., & Liu, Y. (2011). Equilibrium Se isotope fractionation parameters: A first-principles
587 study. *Earth and Planetary Science Letters*, *304*(1), 113–120.
588 https://doi.org/10.1016/j.epsl.2011.01.022
589 Li, X., Zhao, H., Tang, M., & Liu, Y. (2009). Theoretical prediction for several important
590 equilibrium Ge isotope fractionation factors and geological implications. *Earth and*
591 *Planetary Science Letters*, *287*(1), 1–11. https://doi.org/10.1016/j.epsl.2009.07.027
592 Liu, X., Hin, R. C., Coath, C. D., van Soest, M., Melekhova, E., & Elliott, T. (2022).
593 Equilibrium olivine-melt Mg isotopic fractionation explains high δ26Mg values in arc
594 lavas. *Geochemical Perspectives Letters*, *22*, 42–47.
595 https://doi.org/10.7185/geochemlet.2226
596 Liu, X.-N., Hin, R. C., Coath, C. D., Bizimis, M., Su, L., Ionov, D. A., Takazawa, E., Brooker,
597 R., & Elliott, T. (2023). The magnesium isotopic composition of the mantle.
598 *Geochimica et Cosmochimica Acta*, *358*, 12–26.
599 https://doi.org/10.1016/j.gca.2023.08.011
600 Liu (刘效宁), X.-N., Hin, R. C., Coath, C. D., & Elliott, T. (2024). Mg and Fe isotope
601 compositions of mid-ocean ridge basalts modified by Mg-Fe inter-diffusion during melt
602 transport. *Earth and Planetary Science Letters*, *642*, 118868.
603 https://doi.org/10.1016/j.epsl.2024.118868
604 Mallmann, G., & O'Neill, H. St. C. (2009). The Crystal/Melt Partitioning of V during Mantle
605 Melting as a Function of Oxygen Fugacity Compared with some other Elements (Al, P,
606 Ca, Sc, Ti, Cr, Fe, Ga, Y, Zr and Nb). *Journal of Petrology*, *50*(9), 1765–1794.
607 https://doi.org/10.1093/petrology/egp053
608 Méheut, M., & Schauble, E. A. (2014). Silicon isotope fractionation in silicate minerals:
609 Insights from first-principles models of phyllosilicates, albite and pyrope. *Geochimica*
610 *et Cosmochimica Acta*, *134*, 137–154. https://doi.org/10.1016/j.gca.2014.02.014

611 Monkhorst, H. J., & Pack, J. D. (1976). Special points for Brillouin-zone integrations. *Physical*
612 *Review B*, *13*(12), 5188–5192. https://doi.org/10.1103/PhysRevB.13.5188
613 Morse, S. A. (1980). *Basalts and phase diagrams*. Springer.
614 Oeser, M., Dohmen, R., Horn, I., Schuth, S., & Weyer, S. (2015). Processes and time scales of
615 magmatic evolution as revealed by Fe–Mg chemical and isotopic zoning in natural
616 olivines. *Geochimica et Cosmochimica Acta*, *154*, 130–150.
617 https://doi.org/10.1016/j.gca.2015.01.025
618 Pamato, M. G., Nestola, F., Novella, D., Smyth, J. R., Pasqual, D., Gatta, G. D., Alvaro, M., &
619 Secco, L. (2019). The High-Pressure Structural Evolution of Olivine along the
620 Forsterite–Fayalite Join. *Minerals*, *9*(12), Article 12.
621 https://doi.org/10.3390/min9120790
622 Payne, M. C., Teter, M. P., Allan, D. C., Arias, T. A., & Joannopoulos, J. D. (1992). Iterative
623 minimization techniques for ab initio total-energy calculations: Molecular dynamics
624 and conjugate gradients. *Reviews of Modern Physics*, *64*(4), 1045–1097.
625 https://doi.org/10.1103/RevModPhys.64.1045
626 Perdew, J. P., Burke, K., & Ernzerhof, M. (1996). Generalized gradient approximation made
627 simple. *Physical Review Letters*, *77*(18), 3865.
628 Perdew, J. P., Ruzsinszky, A., Csonka, G. I., Vydrov, O. A., Scuseria, G. E., Constantin, L. A.,
629 Zhou, X., & Burke, K. (2008). Restoring the Density-Gradient Expansion for Exchange
630 in Solids and Surfaces. *Physical Review Letters*, *100*(13), 136406.
631 https://doi.org/10.1103/PhysRevLett.100.136406
632 Perdew, J. P., & Zunger, A. (1981). Self-interaction correction to density-functional
633 approximations for many-electron systems. *Physical Review B*, *23*(10), 5048–5079.
634 https://doi.org/10.1103/PhysRevB.23.5048

635 Pogge von Strandmann, P. A. E., Elliott, T., Marschall, H. R., Coath, C., Lai, Y.-J., Jeffcoate,
636 A. B., & Ionov, D. A. (2011). Variations of Li and Mg isotope ratios in bulk chondrites
637 and mantle xenoliths. *Geochimica et Cosmochimica Acta*, *75*(18), 5247–5268.
638 https://doi.org/10.1016/j.gca.2011.06.026
639 Prencipe, M., Tribaudino, M., Pavese, A., Hoser, A., & Reehuis, M. (2000). A SINGLE-
640 CRYSTAL NEUTRON-DIFFRACTION INVESTIGATION OF DIOPSIDE AT 10 K.
641 *The Canadian Mineralogist*, *38*(1), 183–189.
642 https://doi.org/10.2113/gscanmin.38.1.183
643 Putirka, K. D. (2008). Thermometers and barometers for volcanic systems. *Reviews in*
644 *Mineralogy and Geochemistry*, *69*(1), 61–120.
645 Refson, K., Tulip, P. R., & Clark, S. J. (2006). Variational density-functional perturbation
646 theory for dielectrics and lattice dynamics. *Physical Review B*, *73*(15), 155114.
647 https://doi.org/10.1103/PhysRevB.73.155114
648 Richter, F. M., Dauphas, N., & Teng, F.-Z. (2009). Non-traditional fractionation of non-
649 traditional isotopes: Evaporation, chemical diffusion and Soret diffusion. *Chemical*
650 *Geology*, *258*(1), 92–103. https://doi.org/10.1016/j.chemgeo.2008.06.011
651 Richter, F. M., Watson, E. B., Mendybaev, R. A., Teng, F.-Z., & Janney, P. E. (2008).
652 Magnesium isotope fractionation in silicate melts by chemical and thermal diffusion.
653 *Geochimica et Cosmochimica Acta*, *72*(1), 206–220.
654 https://doi.org/10.1016/j.gca.2007.10.016
655 Rustad, J. R., & Dixon, D. A. (2009). Prediction of Iron-Isotope Fractionation Between
656 Hematite (α-Fe2O3) and Ferric and Ferrous Iron in Aqueous Solution from Density
657 Functional Theory. *The Journal of Physical Chemistry A*, *113*(44), 12249–12255.
658 https://doi.org/10.1021/jp9065373

659 Schauble, E. A. (2004). Applying Stable Isotope Fractionation Theory to New Systems.
660 *Reviews in Mineralogy and Geochemistry*, *55*(1), 65–111.
661 https://doi.org/10.2138/gsrmg.55.1.65
662 Schauble, E. A. (2011). First-principles estimates of equilibrium magnesium isotope
663 fractionation in silicate, oxide, carbonate and hexaaquamagnesium(2+) crystals.
664 *Geochimica et Cosmochimica Acta*, *75*(3), 844–869.
665 https://doi.org/10.1016/j.gca.2010.09.044
666 Sedaghatpour, F., & Teng, F.-Z. (2016). Magnesium isotopic composition of achondrites.
667 *Geochimica et Cosmochimica Acta*, *174*, 167–179.
668 https://doi.org/10.1016/j.gca.2015.11.016
669 Sen, G. (1988). Petrogenesis of spinel lherzolite and pyroxenite suite xenoliths from the Koolau
670 shield, Oahu, Hawaii: Implications for petrology of the post-eruptive lithosphere
671 beneath Oahu. *Contributions to Mineralogy and Petrology*, *100*(1), 61–91.
672 https://doi.org/10.1007/BF00399440
673 Sio, C. K. I., Dauphas, N., Teng, F.-Z., Chaussidon, M., Helz, R. T., & Roskosz, M. (2013).
674 Discerning crystal growth from diffusion profiles in zoned olivine by *in situ* Mg–Fe
675 isotopic analyses. *Geochimica et Cosmochimica Acta*, *123*, 302–321.
676 https://doi.org/10.1016/j.gca.2013.06.008
677 Soderman, C. R., Matthews, S., Shorttle, O., Jackson, M. G., Day, J. M. D., Kamenetsky, V.,
678 & Williams, H. M. (2024). Global oceanic basalt sources and processes viewed through
679 combined Fe and Mg stable isotopes. *Earth and Planetary Science Letters*, *638*,
680 118749. https://doi.org/10.1016/j.epsl.2024.118749
681 Stracke, A., Tipper, E. T., Klemme, S., & Bizimis, M. (2018). Mg isotope systematics during
682 magmatic processes: Inter-mineral fractionation in mafic to ultramafic Hawaiian

683 xenoliths. *Geochimica et Cosmochimica Acta*, *226*, 192–205.
684 https://doi.org/10.1016/j.gca.2018.02.002
685 Teng, F.-Z., Dauphas, N., Helz, R. T., Gao, S., & Huang, S. (2011). Diffusion-driven
686 magnesium and iron isotope fractionation in Hawaiian olivine. *Earth and Planetary*
687 *Science Letters*, *308*(3), 317–324. https://doi.org/10.1016/j.epsl.2011.06.003
688 Teng, F.-Z., Li, W.-Y., Ke, S., Marty, B., Dauphas, N., Huang, S., Wu, F.-Y., & Pourmand, A.
689 (2010). Magnesium isotopic composition of the Earth and chondrites. *Geochimica et*
690 *Cosmochimica Acta*, *74*(14), 4150–4166. https://doi.org/10.1016/j.gca.2010.04.019
691 Teng, F.-Z., Wadhwa, M., & Helz, R. T. (2007). Investigation of magnesium isotope
692 fractionation during basalt differentiation: Implications for a chondritic composition of
693 the terrestrial mantle. *Earth and Planetary Science Letters*, *261*(1), 84–92.
694 https://doi.org/10.1016/j.epsl.2007.06.004
695 Teng, F.-Z., Yin, Q.-Z., Ullmann, C. V., Chakrabarti, R., Pogge von Strandmann, P. A. E.,
696 Yang, W., Li, W.-Y., Ke, S., Sedaghatpour, F., Wimpenny, J., Meixner, A., Romer, R.
697 L., Wiechert, U., & Jacobsen, S. B. (2015). Interlaboratory comparison of magnesium
698 isotopic compositions of 12 felsic to ultramafic igneous rock standards analyzed by
699 MC-ICPMS. *Geochemistry, Geophysics, Geosystems*, *16*(9), 3197–3209.
700 https://doi.org/10.1002/2015GC005939
701 Tribaudino, M., Prencipe, M., Bruno, M., & Levy, D. (2000). High-pressure behaviour of Ca-
702 rich C2/c clinopyroxenes along the join diopside-enstatite (CaMgSi2O6-Mg2Si2O6).
703 *Physics and Chemistry of Minerals*, *27*(9), 656–664.
704 https://doi.org/10.1007/s002690000106
705 Urey, H. C. (1947). The thermodynamic properties of isotopic substances. *Journal of the*
706 *Chemical Society (Resumed)*, *0*, 562–581. https://doi.org/10.1039/JR9470000562

Walker, A., Hin, R., & Elliott, T. (2025). *Controls on Mg isotopic fractionation between deep mantle phases and relict signatures of a terrestrial magma ocean*. https://eartharxiv.org/repository/view/9866/

Wang, W., Wu, Z., Huang, S., & Huang, F. (2023). First-principles investigation of equilibrium magnesium isotope fractionation among mantle minerals: Review and new data. *Earth-Science Reviews*, *237*, 104315. https://doi.org/10.1016/j.earscirev.2023.104315

Wu, Z., Huang, F., & Huang, S. (2015). Isotope fractionation induced by phase transformation: First-principles investigation for Mg2SiO4. *Earth and Planetary Science Letters*, *409*, 339–347. https://doi.org/10.1016/j.epsl.2014.11.004

Yang, W., Teng, F.-Z., & Zhang, H.-F. (2009). Chondritic magnesium isotopic composition of the terrestrial mantle: A case study of peridotite xenoliths from the North China craton. *Earth and Planetary Science Letters*, *288*(3), 475–482. https://doi.org/10.1016/j.epsl.2009.10.009

Young, E. D., Manning, C. E., Schauble, E. A., Shahar, A., Macris, C. A., Lazar, C., & Jordan, M. (2015). High-temperature equilibrium isotope fractionation of non-traditional stable isotopes: Experiments, theory, and applications. *Chemical Geology*, *395*, 176–195. https://doi.org/10.1016/j.chemgeo.2014.12.013

Young, E. D., Tonui, E., Manning, C. E., Schauble, E., & Macris, C. A. (2009). Spinel-olivine magnesium isotope thermometry in the mantle and implications for the Mg isotopic composition of Earth. *Earth and Planetary Science Letters*, *288*(3–4), 524–533. https://doi.org/10.1016/j.epsl.2009.10.014

Supplementary Material

The magnitude of equilibrium isotope fractionation of Mg between forsterite, diopside and melt at liquidus temperatures.

Bram de Winter, Department of Earth Sciences, Department of Earth Sciences, University of Oxford, South Parks Road, Oxford, OX1 3AN, UK

1. Experiments

Fig. S1-1. SEM pictures of samples with composition BDW-S1 and BDW-S2

BDW-S1 composition

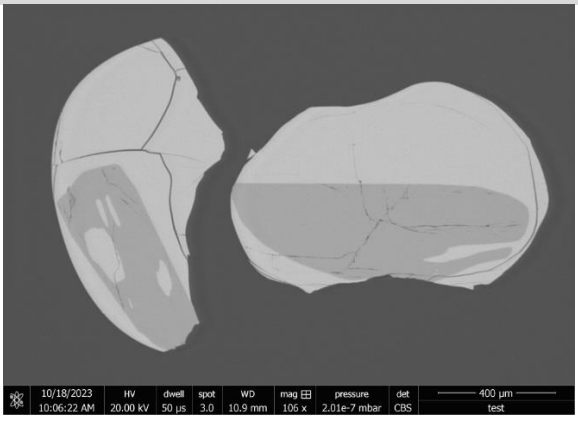

BDW-S1-1

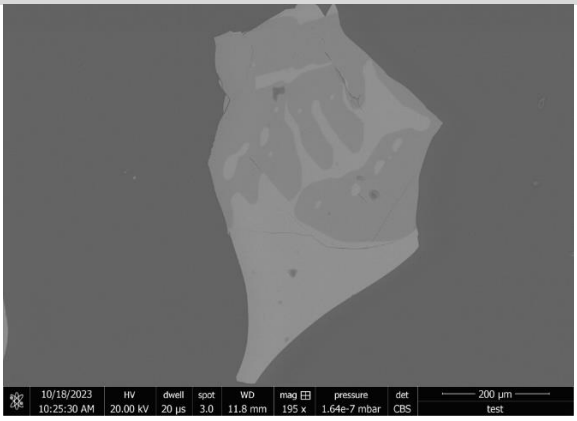

BDW-S1-2

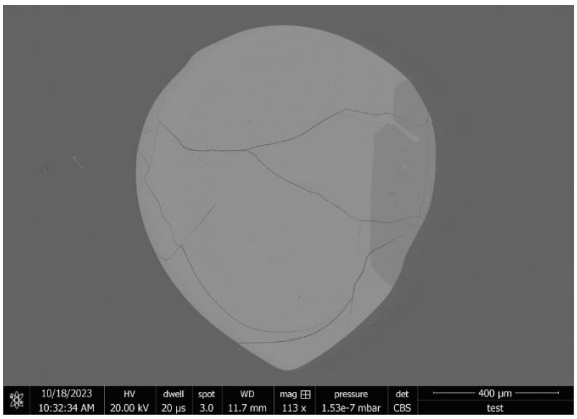

BDW-S1-3

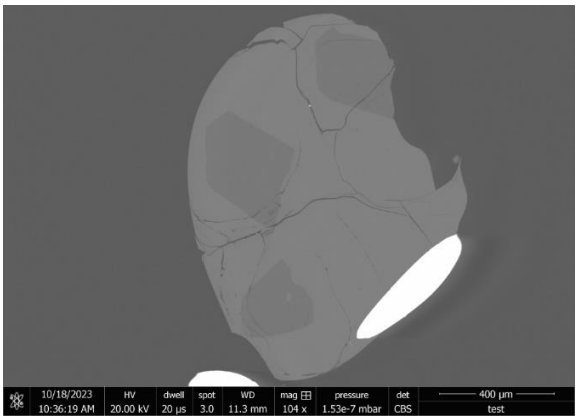

BDW-S1-4

BDW-S2 Composition

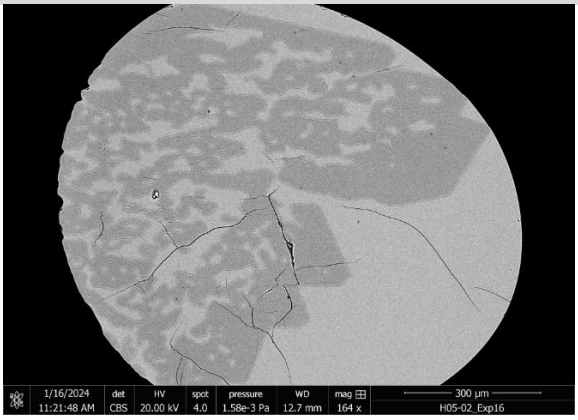

BDW-S2-1

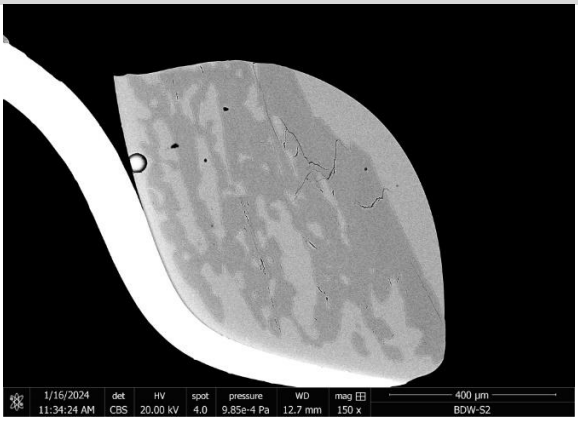

BDW-S2-3

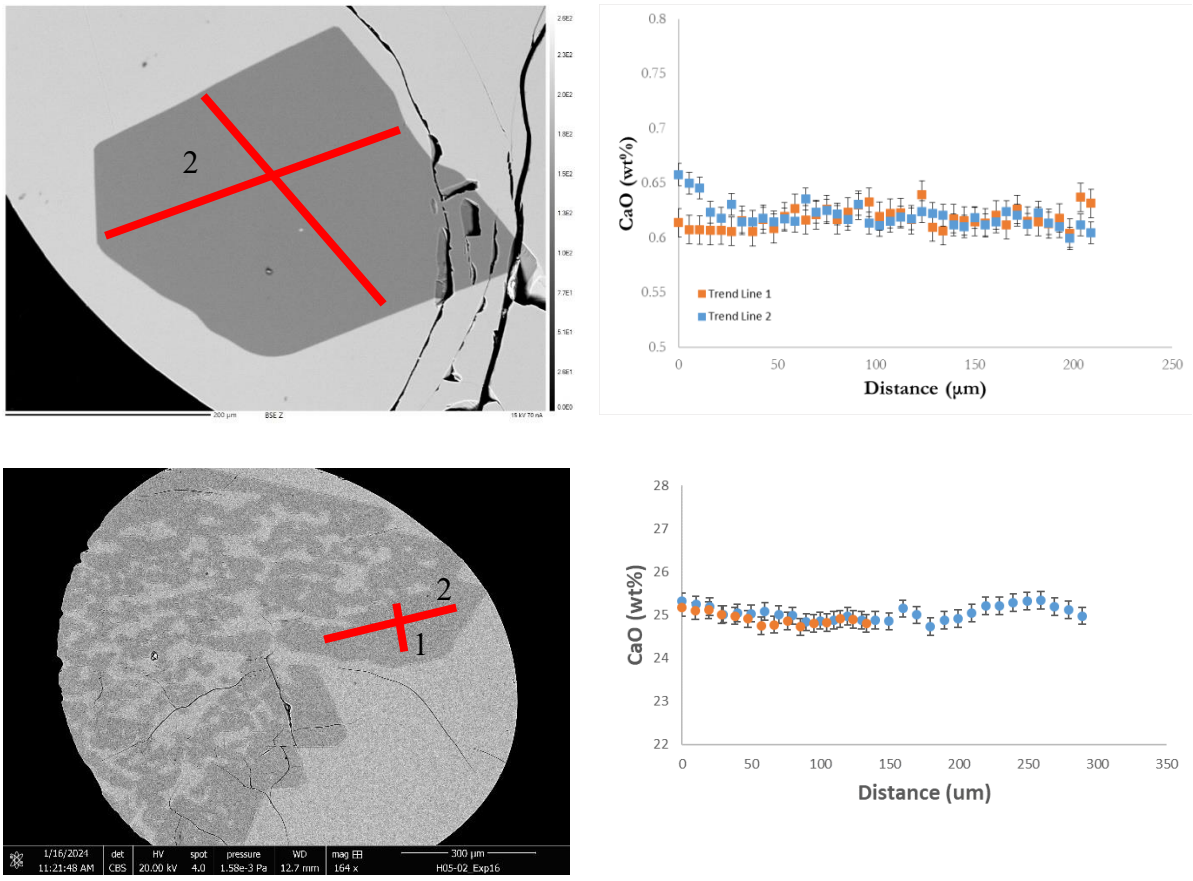

Fig. S1-2 a) EMPA picture with highlighted lines that represent measurement analysis line stages through the forsterite crystal. Analyses were performed every 10 µm with a spot size of 5 µm. B) Concentration of CaO versus distance on the cross-section line stages. C) EMPA picture diopside crystal. D) Concentration of CaO versus distance on the cross-section line stages in diopside.

1.1 Experimental isotope analysis

Table S1-1, Individual δ^{26}Mg measurements (‰) for olivine (Ol), diopside (Di), and coexisting melt from experiments BDW-S1-4 (Fo) and BDW-S2-1 (Di). Error bars represent two standard errors (2 s.e.).

Experiment	Drill site	Phase	δ^{26}Mg	2 s.e.	n[a]
BDW-S1-4 (Fo)					
	A	Ol	-1.427	0.035	9
	B	Melt	-1.347	0.035	9
	C	Melt	-1.366	0.035	9
	D	Ol	-1.413	0.035	9

	E	Melt	-1.381	0.035	9
	F	Melt	-1.354	0.035	9
BDW-S2-1 (Di)					
	A	Di	-1.312	0.023	12
	B	Melt	-1.361	0.023	6
	C	Melt	-1.338	0.023	6

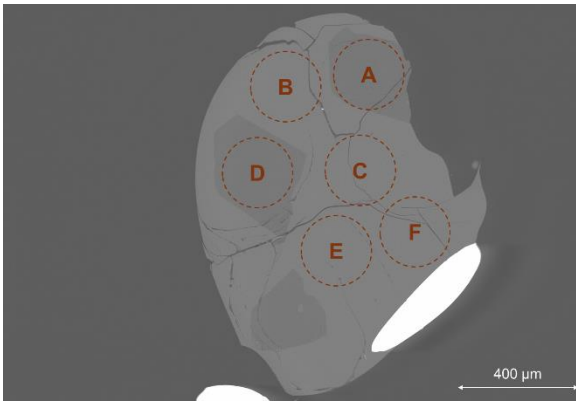

BDW-S1-4 (Fo)

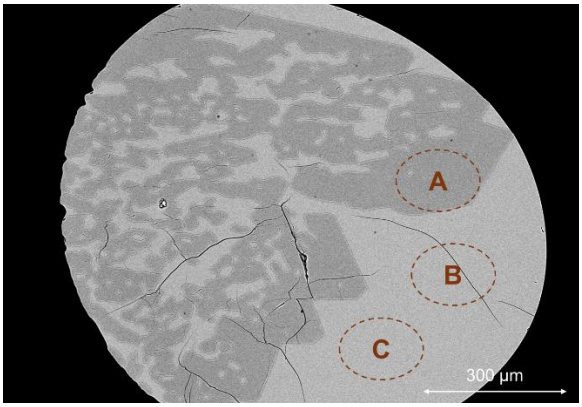

BDW-S2-1 (Di)

1.2 Literature data (simple bracketing)

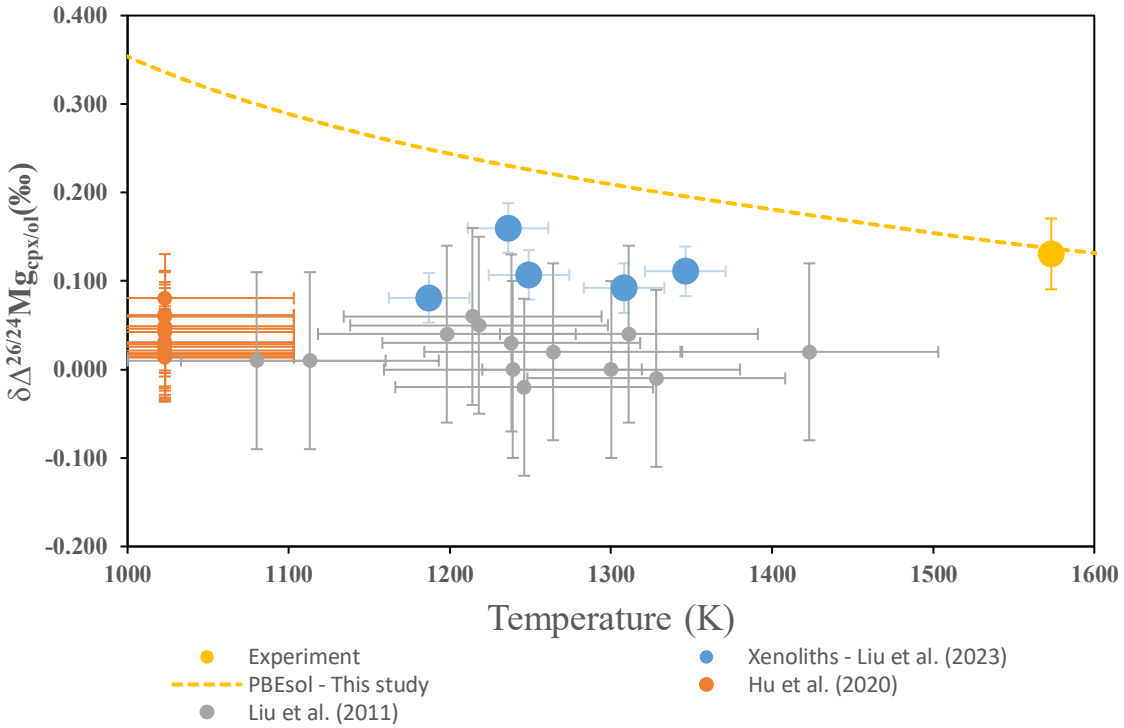

Figure S1-3, Compilation of literature data where both $\Delta^{26}Mg_{cpx/ol}$ and temperature of formation have been estimated. Note the large error bars on Hu et al. (2020) and Liu et al. (2011) compared to the double-spiking methods of Liu et al. (2023).

2. Ab initio calculations

Minerals		Mg-O
Forsterite	LDA	2.0587
	GGA	2.0962
	PBESOL	2.0802
Diopside	LDA	2.0189
	GGA	2.0761
	PBESOL	2.0565

Table S2-1 Average Mg-O and Si-O bonds in Å, for 0 GPa calculations performed for diopside and forsterite mineral cells using LDA, GGA and PBESOL exchange-correlation functionals.

Table S2-2, unit cell parameters and static volume at 0 K for different E_{xc} used in this study and literature studies. *Ab initio* studies are compared with experimentally determined unit cell volume parameters. Experiments are extrapolated towards 0 K unit cell parameters.

	E_{xc}	**a**	**b**	**c**	**static volume (Å^3)**	
Forsterite	LDA	4.732	10.101	5.933	283.584	this study
	LDA	4.738	10.115	5.941	284.714	Huang et al. (2013)
	GGA	4.814	10.357	6.067	302.491	this study
	GGA	4.790	10.303	6.036	297.885	Schauble (2011)
	PBESOL	4.777	10.241	6.008	293.948	this study
	Experiments	4.758	10.190	5.982	290.000	Pamato et al. (2019)
Diopside	LDA	9.687	8.781	5.015	427.101	this study
	LDA	9.692	8.835	5.213	430.477	Wang et al. (2023)
	GGA	9.918	9.043	5.128	459.524	this study
	GGA	9.879	8.986	5.308	451.844	Schauble (2011)
	PBESOL	9.802	8.917	5.070	443.353	this study
	Experiments	9.749	8.925	5.252	439.465	Tribaudino et al. (2000)

Table S2-3, Polynomial fitted constants for 1000 ln (ß (X, ^{24}Mg, ^{26}Mg) = $AT^{-6}+BT^{-4}+CT^{-2}$ as a function of T in Kelvin for different studies with 1000lnß at 1000 K.

Mineral	E_{xc}	Study	T-exp	Site averaging	Polynomial fits (static) 1000ln(ß) = $Ax+Bx^2+Cx^3$			1000ln(ß) (1000K)
					A	B	C	
Diopside	LDA	Wang et al. (2023)	Yes	N/A	2.767	-0.01812	0.0001877	2.7487
Diopside	LDA	Huang et al. (2013)	No	N/A	2.2442	0.1052	-0.0117	2.3353*
Diopside	B3LYP	Gao et al. (2018)	No	N/A	2.5287	-0.014671	0.00012343	2.5142
Diopside	PBE	Duan et al. (2023)	No	No	2.3365	−0.01415	0.0001	2.3235
Forsterite	LDA	Wang et al. (2023)	Yes	No	2.565	-0.01735	0.0001947	2.5478
Forsterite	LDA	Huang et al. (2013)	No	No	2.0748	0.1052	-0.0119	2.1681*
Forsterite	LDA	Wu et al. (2015)	No	No	-0.108	2.29	0.0094	2.1914
Forsterite	B3LYP	Gao et al. (2018)	No	No	2.387	-0.015128	0.00014897	2.3720
Forsterite	PBE	Duan et al. (2023)	No	Yes	2.4265	−0.01555	0.00015	2.4111
					1000ln(ß) = $AT^{-6}+BT^{-4}+CT^{-2}$			
					A	B	C	
Forsterite	PBESOL	This Study	Yes	Yes	2.61×10^{14}	-1.64×10^{10}	2.35×10^{6}	2.3964
Forsterite	PBE	This Study	Yes	Yes	1.43×10^{14}	-1.43×10^{10}	2.32×10^{6}	2.2315
Forsterite	LDA	This Study	Yes	Yes	2.45×10^{14}	-1.54×10^{10}	2.25×10^{6}	2.5642
Diopside	PBESOL	This Study	Yes	N/A	2.16×10^{14}	-1.57×10^{10}	2.52×10^{6}	2.5024
Diopside	PBE	This Study	Yes	N/A	1.54×10^{14}	-1.22×10^{10}	2.19×10^{6}	2.1763
Diopside	LDA	This Study	Yes	N/A	2.72×10^{14}	-1.88×10^{10}	2.78×10^{6}	2.7647
Diopside	PBE	Schauble et al. (2011)	No	N/A	1.4032×10^{14}	-1.4915×10^{10}	2.4806×10^{6}	2.4658
Forsterite	PBE	Schauble et al. (2011)	No	Yes	1.5614×10^{14}	-1.5115×10^{10}	2.3547×10^{6}	2.3397
Forsterite	PBE	Walker et al. (2025)	Yes	No	1.8414×10^{14}	-1.6279×10^{10}	2.4312×10^{6}	2.4151

*Huang et al. (2013) polynomials provide different 1000 K 1000lnß compared to their provided supplementary data

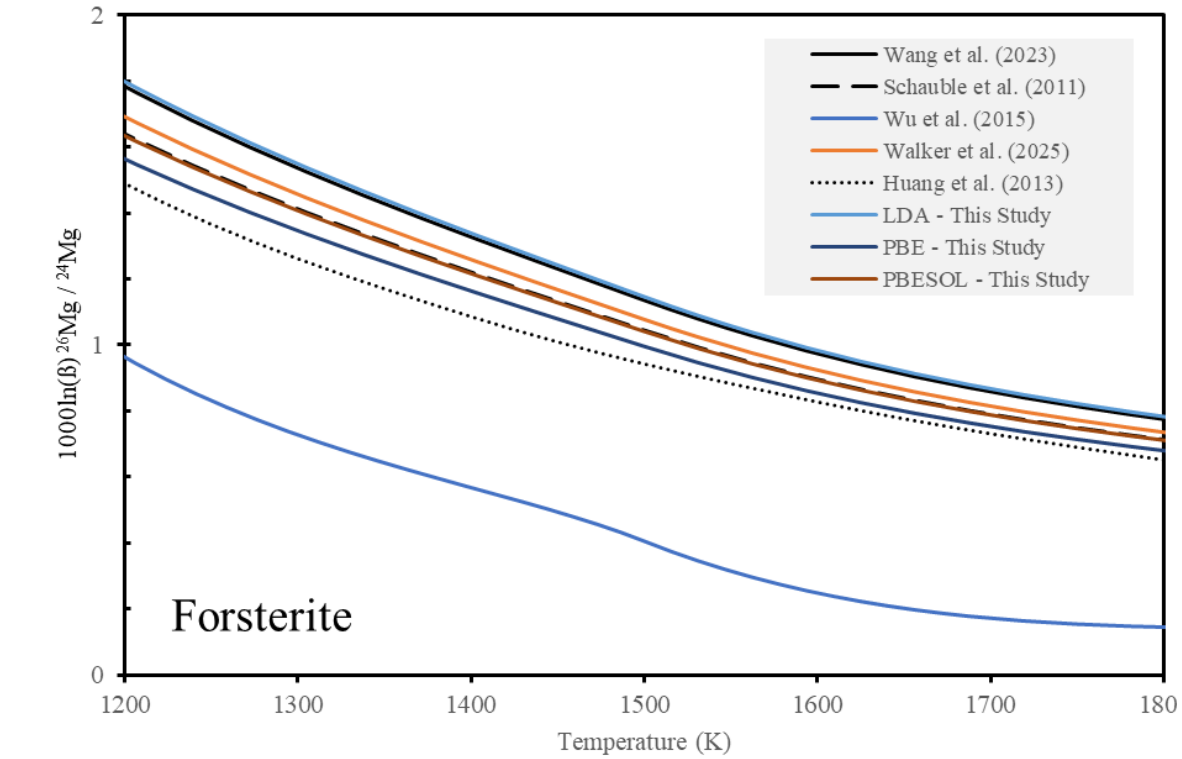

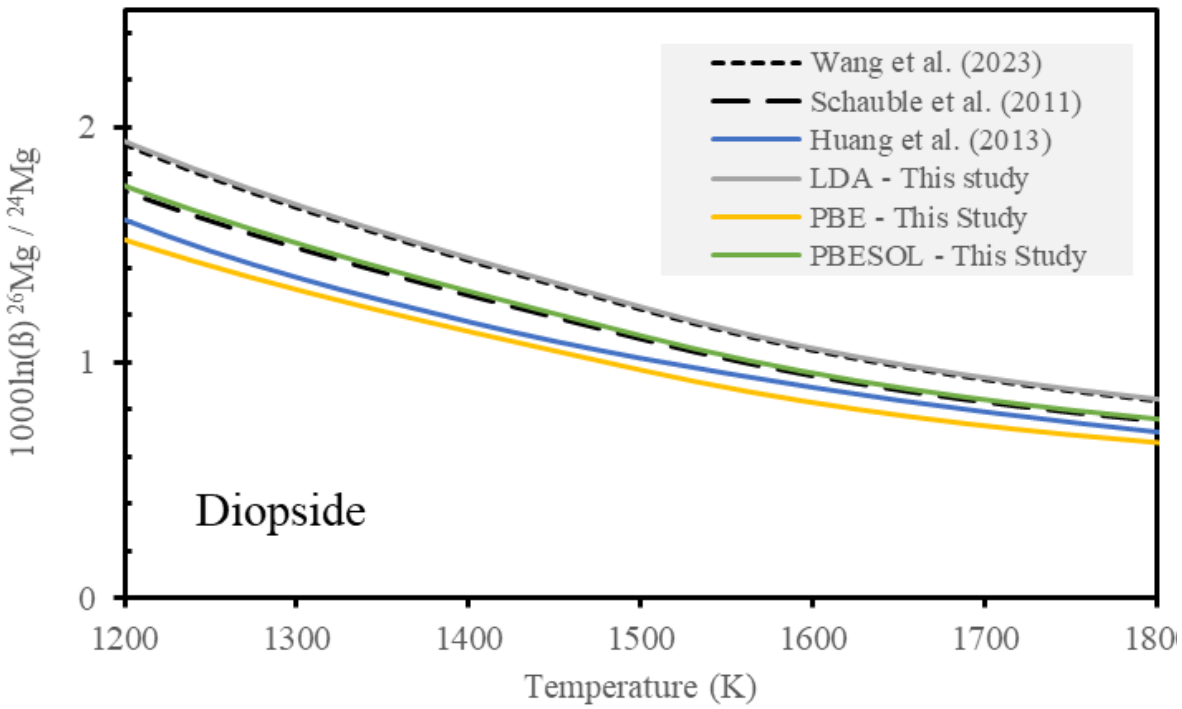

Figure S2-1 , Reduced partitioning function for magnesium isotopes in a) forsterite and b) Diopside. An overview of the literature is given in the Supplementary table S2-3

		Forsterite	**Diopside**
F0	x0	-8.96×10^3	-1.68×10^4

	x1	1.06×10^{-3}	9.80×10^{-4}
	x2	-9.68×10^{-6}	-1.33×10^{-5}
	x3	2.85×10^{-9}	3.95×10^{-9}
	x4	-5.15×10^{-13}	-7.16×10^{-13}
	x5	3.61×10^{-17}	5.40×10^{-17}
V0	x0	2.96×10^{2}	4.47×10^{2}
	x1	1.18×10^{-2}	7.31×10^{-3}
	x2	1.48×10^{-5}	-1.06×10^{-5}
	x3	1.83×10^{-8}	1.65×10^{-8}
	x4	-7.20×10^{-12}	-5.98×10^{-12}
	x5	9.99×10^{-16}	6.56×10^{-16}
K0	x0	1.22×10^{2}	9.70×10^{1}
	x1	-8.41×10^{-3}	-1.65×10^{-3}
	x2	-1.85×10^{-5}	-4.72×10^{-5}
	x3	1.03×10^{-8}	-2.72×10^{-10}
	x4	-2.89×10^{-12}	6.84×10^{-12}
	x5	2.86×10^{-15}	-1.11×10^{-15}
K'0	x0	4.35	7.06
	x1	1.88×10^{-3}	2.92×10^{-1}
	x2	-4.60×10^{-6}	-9.88×10^{-4}
	x3	4.17×10^{-9}	9.48×10^{-7}
	x4	-1.48×10^{-12}	-3.08×10^{-10}
	x5	1.85×10^{-16}	3.24×10^{-14}

Table S2-4, Birch-Murnaghan equation of state (EOS) for forsterite and diopside using PBESOL exchange-correlation functional. Parameters can be fitted to V using equation 1:

$$F(V) = F_0 + \frac{9V_0K_0}{16}\left\{\left[\left(\frac{V_0}{V}\right)^{\frac{2}{3}} - 1\right]^3 K_0' + \left[\left(\frac{V_0}{V}\right)^{\frac{2}{3}} - 1\right]^2 \left[6 - 4\left(\frac{V_0}{V}\right)^{\frac{2}{3}}\right]\right\} \qquad (1)$$

	Forsterite M1	**Forsterite M2**	**Forsterite average**	**Diopside**
A1	-1.64×10^{15}	-1.41×10^{15}	-1.53×10^{15}	-9.44×10^{14}
A2	5.64×10^{17}	4.85×10^{17}	5.25×10^{17}	5.15×10^{17}
B1	-1.35×10^{11}	-1.16×10^{11}	-1.26×10^{11}	-2.81×10^{11}

B2	9.82×10^{13}	8.45×10^{13}	9.13×10^{13}	2.76×10^{13}
B3	-1.88×10^{16}	-1.62×10^{16}	-1.75×10^{16}	-7.02×10^{16}
C1	1.28×10^{6}	1.10×10^{6}	1.19×10^{6}	9.57×10^{6}
C2	-1.46×10^{9}	-1.26×10^{9}	-1.36×10^{9}	-9.79×10^{9}
C3	5.41×10^{11}	4.65×10^{11}	5.03×10^{11}	2.95×10^{12}

Table S2-5, Fitted parameters with thermal expansion correction. 1000 ln (beta) can be found using equation 2:

$$1000 \ln \beta(V,T) = (A_1 + A_2 V^{-1})T^{-6} + (B_1 + B_2 V^{-1} + B_3 V^{-2})T^{-4} + (C_1 + C_2 V^{-1} + C_3 V^{-2})T^{-2} \quad (2)$$

References

Gao, C., Cao, X., Liu, Q., Yang, Y., Zhang, S., He, Y., Tang, M., & Liu, Y. (2018). Theoretical calculation of equilibrium Mg isotope fractionations between minerals and aqueous solutions. *Chemical Geology*, *488*, 62–75. https://doi.org/10.1016/j.chemgeo.2018.04.005

Hu, Y., Teng, F.-Z., & Ionov, D. A. (2020). Magnesium isotopic composition of metasomatized upper sub-arc mantle and its implications to Mg cycling in subduction zones. *Geochimica et Cosmochimica Acta*, *278*, 219–234. https://doi.org/10.1016/j.gca.2019.09.030

Huang, F., Wu, Z., Huang, S., & Wu, F. (2014). First-principles calculations of equilibrium silicon isotope fractionation among mantle minerals. *Geochimica et Cosmochimica Acta*, *140*, 509–520. https://doi.org/10.1016/j.gca.2014.05.035

Liu, S.-A., Teng, F.-Z., Yang, W., & Wu, F.-Y. (2011). High-temperature inter-mineral magnesium isotope fractionation in mantle xenoliths from the North China craton. *Earth and Planetary Science Letters*, *308*(1), 131–140. https://doi.org/10.1016/j.epsl.2011.05.047

Liu, X.-N., Hin, R. C., Coath, C. D., Bizimis, M., Su, L., Ionov, D. A., Takazawa, E., Brooker, R., & Elliott, T. (2023). The magnesium isotopic composition of the mantle. *Geochimica et Cosmochimica Acta*, *358*, 12–26. https://doi.org/10.1016/j.gca.2023.08.011

Schauble, E. A. (2011). First-principles estimates of equilibrium magnesium isotope fractionation in silicate, oxide, carbonate and hexaaquamagnesium(2+) crystals. *Geochimica et Cosmochimica Acta*, *75*(3), 844–869. https://doi.org/10.1016/j.gca.2010.09.044

Walker, A., Hin, R., & Elliott, T. (2025). *Controls on Mg isotopic fractionation between deep mantle phases and relict signatures of a terrestrial magma ocean*. https://eartharxiv.org/repository/view/9866/

Wang, W., Wu, Z., Huang, S., & Huang, F. (2023). First-principles investigation of equilibrium magnesium isotope fractionation among mantle minerals: Review and new data. *Earth-Science Reviews*, *237*, 104315. https://doi.org/10.1016/j.earscirev.2023.104315

Wu, Z., Huang, F., & Huang, S. (2015). Isotope fractionation induced by phase transformation: First-principles investigation for Mg2SiO4. *Earth and Planetary Science Letters*, *409*, 339–347. https://doi.org/10.1016/j.epsl.2014.11.004